nature cell biology

Article

https://doi.org/10.1038/s41556-023-01314-6

Gut microbial metabolite facilitates colorectal cancer development via ferroptosis inhibition

Received: 23 September 2022

Accepted: 15 November 2023

Published online: 2 January 2024

Check for updates

Weiwei Cui[1,13], Meng Guo[2,13], Dong Liu[1,13], Peng Xiao[1], Chuancheng Yang[1], Haidi Huang[3], Chunhui Liang[1], Yinghong Yang[1], Xiaolong Fu[4], Yudan Zhang[1], Jiaxing Liu[1], Shuang Shi[5], Jingjing Cong[2], Zili Han[2], Yunfei Xu[6], Lutao Du[6], Chengqian Yin[7], Yongchun Zhang[3], Jinpeng Sun[1], Wei Gu[8] ✉, Renjie Chai[4,9,10,11] ✉, Shu Zhu[2,12] ✉ & Bo Chu[1] ✉

The gut microbiota play a pivotal role in human health. Emerging evidence indicates that gut microbes participate in the progression of tumorigenesis through the generation of carcinogenic metabolites. However, the underlying molecular mechanism is largely unknown. In the present study we show that a tryptophan metabolite derived from *Peptostreptococcus anaerobius*, *trans*-3-indoleacrylic acid (IDA), facilitates colorectal carcinogenesis. Mechanistically, IDA acts as an endogenous ligand of an aryl hydrocarbon receptor (AHR) to transcriptionally upregulate the expression of *ALDH1A3* (aldehyde dehydrogenase 1 family member A3), which utilizes retinal as a substrate to generate NADH, essential for ferroptosis-suppressor protein 1(FSP1)-mediated synthesis of reduced coenzyme Q10. Loss of AHR or *ALDH1A3* largely abrogates IDA-promoted tumour development both in vitro and in vivo. It is interesting that *P. anaerobius* is significantly enriched in patients with colorectal cancer (CRC). IDA treatment or implantation of *P. anaerobius* promotes CRC progression in both xenograft model and Apc$^{Min/+}$ mice. Together, our findings demonstrate that targeting the IDA–AHR–*ALDH1A3* axis should be promising for ferroptosis-related CRC treatment.

Accumulating studies show that the gut microbiota maintain the balance of metabolism[1]. Dysregulation of the gut microbiota contribute to the pathogenesis of various diseases, including inflammation and infection, gastrointestinal diseases and tumorigenesis[2–4]. The gut microbiome produces a diverse metabolite repertoire from dietary undigested components as well as from host-derived endogenous compounds. Emerging evidence indicates that gut microbes participate in the progression of tumorigenesis through the generation of carcinogenic microbial metabolites[5–7]. However, little is known about the underlying mechanism by which gut microbial metabolites regulate tumorigenesis.

Ferroptosis, a new type of cell death distinct from apoptosis and necrosis, is induced by accumulated peroxidized phospholipids in an iron-dependent manner[8–11]. Ferroptosis is tightly regulated by glutathione peroxidase 4 (GPX4), ferroptosis-suppressor protein 1 (FSP1), a tetrahydrobiopterin (BH4) system or newly identified dihydro-orotate dehydrogenase (DHODH) via converting lipid hydroperoxides (poly(unsaturated fat) (PUFA)-OOH) into non-toxic lipid alcohols (PUFA-OH)[11–15]. Increasing studies indicate that ferroptosis is implicated in cancer immunotherapy and tumour suppression[16–19] and multiple endogenous metabolites could regulate ferroptosis[20,21]. These data led

A full list of affiliations appears at the end of the paper. ✉e-mail: wg8@cumc.columbia.edu; renjiec@seu.edu.cn; zhushu@ustc.edu.cn; chubo123@sdu.edu.cn

us to explore whether gut microbial metabolites mediate colorectal carcinogenesis through ferroptosis.

In the present study, we demonstrated the role of IDA-mediated CRC development. Our studies revealed that a derivative of tryptophan, IDA, but not any other tryptophan metabolites, promotes tumour development through ferroptosis inhibition both in vitro and in vivo. Specifically, IDA-mediated ferroptotic resistance of cancer cells is dependent on the AHR–*ALDH1A3*–FSP1 axis. IDA supplementation or implantation of *P. anaerobius* promotes tumour progression, implicating disruption of the IDA–AHR–*ALDH1A3*–FSP1 pathway possibly being beneficial for CRC treatment.

Results

Identification of IDA as a potent ferroptosis suppressor

To test whether gut microbiota metabolites impact ferroptotic sensitivity of cancer cells, we performed a screening library containing 350 endogenous human host and gut microbe metabolites for ferroptosis assay in 786-O human kidney adenocarcinoma cells (Fig. 1a). It is interesting that our screen data identified IDA, generated from tryptophan metabolism by intestinal microbiota, which significantly inhibited RSL3-induced ferroptosis (Fig. 1b). To validate this finding, two classic ferroptosis-sensitive cancer cell lines, 786-O and HT1080 human fibrosarcoma cells, were utilized to test the effect of IDA and found that cells treated with IDA were robustly resistant to ferroptosis (Fig. 1c,d and Extended Data Fig. 1a,b). Indole-3-propionic acid (IPA), included in the library, is the downstream metabolite of IDA. However, IPA exhibits no protective effect against ferroptosis in 786-O and HT1080 cells (Extended Data Fig. 1c,d), whereas IDA significantly inhibited ferroptotic cell death (Extended Data Fig. 1e–g). We also examined the levels of lipid peroxidation in IDA-incubated HT1080 cells and found that IDA markedly decreased lipid peroxidation (Fig. 1e and Extended Data Fig. 1h), indicating that IDA is a potent ferroptosis suppressor.

The gut microbiota utilize tryptophan to synthesize a variety of derivates (Extended Data Fig. 1i), so we investigated whether other gut microbe-derived tryptophan metabolites could regulate ferroptosis. It is interesting that supplementation of IDA at 10 μM efficiently abrogated ferroptotic cell death in HT1080 cells, whereas low doses (10–100 μM) of other tryptophan derivates displayed no strong protective effect (Fig. 1f and Extended Data Figs. 1j–p and 2a). Furthermore, supplementation with IDA, but not any other tryptophan metabolites, greatly abolished ferroptosis in HT29 human colon cancer cells (Fig. 1g and Extended Data Fig. 2b). As IDA is more efficient at suppressing ferroptosis, we therefore focused our attention on IDA-mediated ferroptosis inhibition. High levels of ferroptotic cell death and lipid peroxidation were remarkably inhibited on IDA treatment in HT29 cells and MC38 mouse colon cancer cells (Fig. 1h–k and Extended Data Fig. 2c). To examine whether IDA acts as radical-trapping antioxidants (RTAs) to inhibit ferroptosis, we predicted the lipophilicity of all the tryptophan metabolites and examined their activity in capturing free radicals by 2,2-diphenyl-1-picrylhydrazyl (DPPH) and fluorescence-enabled inhibited autoxidation (FENIX) assays (Extended Data Fig. 2d,e). These data showed that IDA is unable to directly diminish oxidized lipids (Fig. 1l), suggesting that IDA might mediate ferroptosis through the cellular signalling pathway.

IDA facilitates colorectal tumour development

As in vitro two-dimensional cell culture lacks many features of cancers, such as hypoxia, altered cell–cell contacts and rewired metabolism, we cultured HT29 and MC38 cells into three-dimensional (3D) tumour spheroids to better mimic the in vivo context. As shown in Fig. 2a,b and Extended Data Fig. 2f, RSL3- or imidazole ketone erastin (IKE)-induced ferroptosis in HT29 tumour spheroids was largely inhibited by supplementation of IDA or liprostatin-1 (Lipro-1). Consistently, similar findings were observed in MC38 3D tumour spheroids (Extended Data Fig. 2g) and HT29 organoids (Fig. 2c,d and Extended Data Fig. 2h).

To ascertain whether IDA exhibits protective effect on tumour progression, we performed an HT29 xenograft and found that IDA remarkably abolished lipid peroxidation and promoted tumour development (Fig. 2e–g). In line with this finding, IDA showed strong protection against ferroptosis and promoted MC38 xenograft progression in C57BL/6J mice (Fig. 2h–j). In addition, we performed pharmacokinetic studies of IDA via administration of 50 mg kg^{-1} of IDA intraperitoneally (i.p.) and found that the highest level of IDA in plasma reached about 10 μM (Extended Data Fig. 2i), indicating that a low concentration of IDA in vivo is sufficient to promote tumour progression via ferroptosis inhibition.

AHR is required for IDA-mediated ferroptosis inhibition

Previous research revealed that indole metabolites are naive ligands of AHR[22]. To ascertain whether AHR is involved in IDA-regulated ferroptosis inhibition, we used AHR antagonists BAY-218 and StemRegenin 1 (SR1) (Extended Data Fig. 3a) and found that AHR antagonists remarkably abrogated IDA-modulated ferroptosis inhibition (Fig. 3a and Extended Data Fig. 3b). We next silenced the gene expression in HT29 and HT1080 cells (Fig. 3b and Extended Data Fig. 3c). As expected, IDA failed to inhibit ferroptosis in the cells expressing small hairpin (sh)-AHR (Fig. 3c and Extended Data Fig. 3d). Furthermore, we knocked out AHR via clustered irregularly spaced short palindromic repeats (CRISPR)–Cas9 technology (Fig. 3d and Extended Data Fig. 3e). Indeed, given the lack of AHR expression, IDA failed to rescue ferroptotic cell death (Fig. 3e,f and Extended Data Fig. 3f,g). Similar results were observed in MC38 cells transfected with AHR small interfering RNA (siRNA) (Extended Data Fig. 3h–j).

We further generated $AHR^{-/-}$ clones in HT29 and HT1080 cells in which we observed no alteration in the level of cell proliferation (Extended Data Fig. 3k–n). Consistent with the aforementioned data, ferroptosis in $AHR^{-/-}$ clones was not rescued by IDA (Extended Data Fig. 3o,p). Moreover, IDA-mediated ferroptosis inhibition in AHR^{null} HT29 cells was restored by ectopic expression of AHR (Fig. 3g–j). In agreement with this finding, similar data were achieved in $AHR^{-/-}$ HT1080 cells (Extended Data Fig. 3q–s). A recent work declared that kynurenine, which is another metabolite of tryptophan, inhibits ferroptosis dependent on NRF2, but independent of AHR[21]. We compared the cell viability of AHR or NRF2 knockout (KO) cells on ferroptosis induction. AHR KO significantly blocked low or high concentrations of IDA-mediated ferroptosis inhibition, whereas NRF2 KO exhibited an incapacity to abolish the protective effect of IDA (Extended Data Fig. 3t). To examine whether AHR contributes to IDA-mediated tumour development in vivo, we performed wild-type (WT) and AHR KO HT29 xenograft assay and confirmed that the protective effect of IDA was largely abrogated in $AHR^{-/-}$ cells (Fig. 3k–n).

AHR–ligand interaction promotes AHR translocation to the nucleus and induces the expression of a variety of target genes[22]. To test whether IDA is an endogenous ligand of AHR, we performed a bioluminescence resonance energy transfer (BRET) assay and confirmed that IDA is an endogenous ligand of AHR (Extended Data Fig. 4a–c). Further experiments revealed that nucleus translocation of AHR was more remarkable on IDA treatment and IDA exhibited higher expression of AHR's target genes (Extended Data Fig. 4d–f), indicating that AHR might prefer IDA for ferroptosis resistance. We next constructed a ligand-binding domain (LBD)- and transcriptional activation domain (TAD)-deficient mutant AHR expression vector (Extended Data Fig. 4g,h) and found that IDA-mediated ferroptosis inhibition in AHR^{null} HT1080 cells was restored by ectopic expression of WT AHR but not by the LBD or TAD mutant (Extended Data Fig. 4i). According to computational docking and references, we found that AHR has multiple potential sites for IDA binding. To validate which binding site of AHR is required for the function of IDA, we detected the effects of these mutations (Extended Data Fig. 4j). As shown in Extended Data Fig. 4k,l, WT AHR restored IDA-induced expression of cytochrome P450 family 1 subfamily A

https://doi.org/10.1038/s41556-023-01314-6

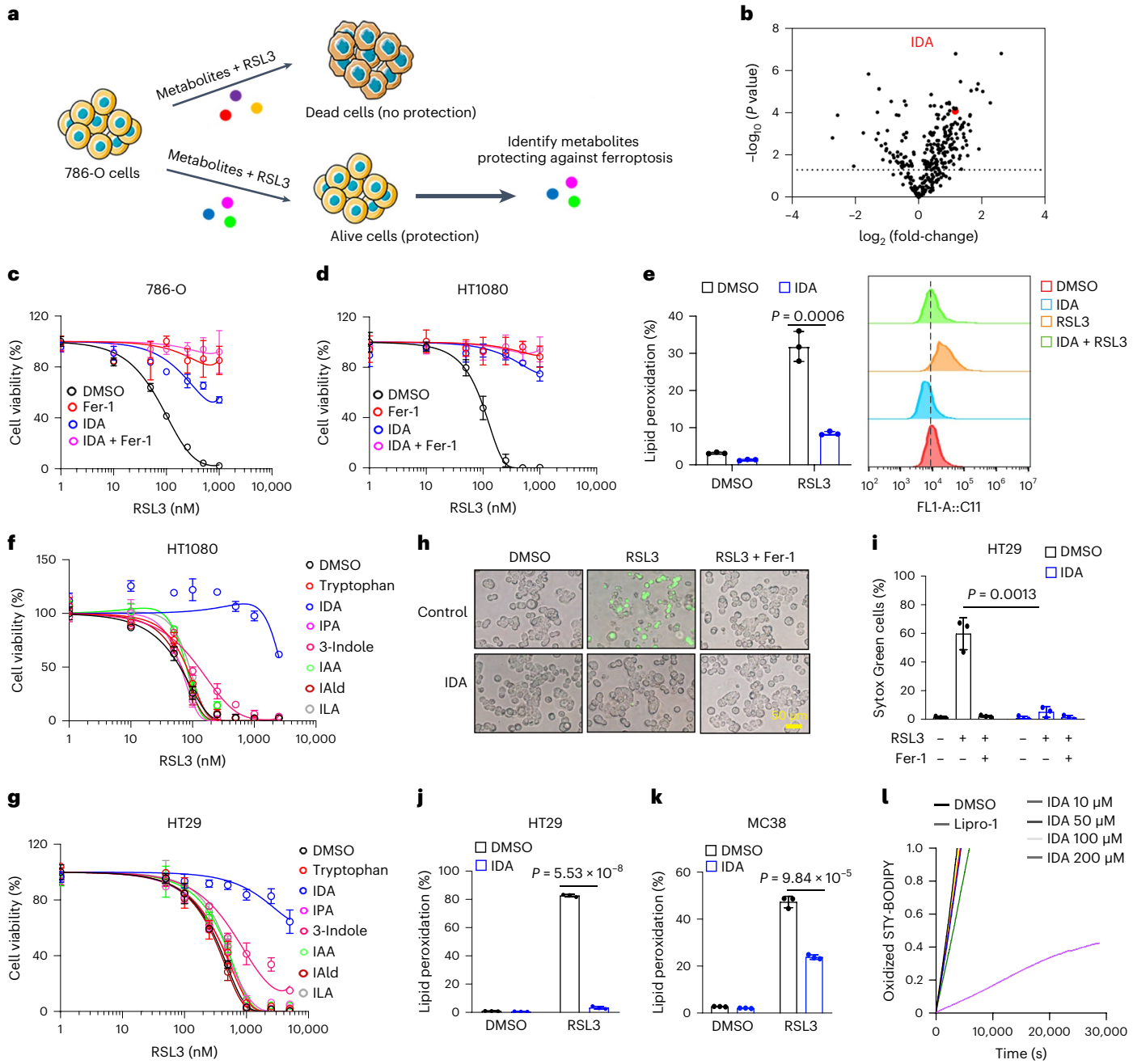

Fig. 1 | Identification of IDA as a potent ferroptosis suppressor. a, Schematic of the identification of potential ferroptosis-induced metabolites generated by gut microbes, using 786-O cells pretreated with endogenous metabolites followed by RSL3 treatment for 24 h. **b**, Volcano plots showing the top hits of an endogenous metabolite screen in 786-O cells, highlighting IDA as a ferroptosis inhibitor. **c**,**d**, Dose-dependent toxicity of RSL3-induced cell death of 786-O (**c**) and HT1080 (**d**) cells supplemented with IDA (50 μM) and Fer-1 (1 μM). Cell viability was assessed 24 h thereafter using CCK8. **e**, C11-BODIPY 581/591 staining of lipid peroxidation in HT1080 cells treated with RSL3 (200 nM) or IDA (50 μM) for 4 h. **f**,**g**, Cell viability in HT1080 (**f**) and HT29 (**g**) cells treated with RSL3 and the indicated tryptophan metabolites for 24 h: tryptophan (50 μM), IDA (50 μM), IPA (50 μM), 3-indole (50 μM), IAA (50 μM), IAld (50 μM) and ILA (50 μM). **h**,**i**, Representative phase-contrast images of HT29 cells (**h**) incubated with IDA (50 μM) treated with RSL3 (5 μM) and Fer-1 (1 μM) for 12 h. Dead cells were stained with Sytox Green (**i**). Scale bars, 50 μm. **j**,**k**, Lipid peroxidation in HT29 (**j**) and MC38 (**k**) colon cancer cells treated with RSL3 (5 μM) and IDA (50 μM) for 4 h. **l**, FENIX assay to determine lipid radical-trapping activity of indicated concentration of IDA. Liprostatin-1 was used as a positive control. Data and error bars are mean ± s.d., $n = 3$ biological independent experiments in **c**–**g** and **i**–**k**. All P values were calculated using two-tailed, unpaired Student's t-test.

member 2 (*CYP1A2*) and protection against ferroptosis, whereas the effect was impaired in some mutations tested (especially Gln323Ala, Ser365Ala and Glu393Ala), suggesting that these sites are critical for IDA–AHR interaction and consequent activation of AHR. Taken together, these findings demonstrate that the IDA–AHR interaction plays a fundamental role in IDA-promoted ferroptosis resistance.

FSP1 is required for the anti-ferroptotic effect of IDA

An IDA-induced AHR cascade was reported to activate nucleus factor-erythroid 2-related factor-2 (NFE2L2, also known as NRF2)[23]. In addition, analysis of public chromatin immunoprecipitation sequencing (ChIP–seq) data of AHR revealed that NRF2 is a potential target of AHR (Extended Data Fig. 5a), suggesting that the IDA–AHR

https://doi.org/10.1038/s41556-023-01314-6

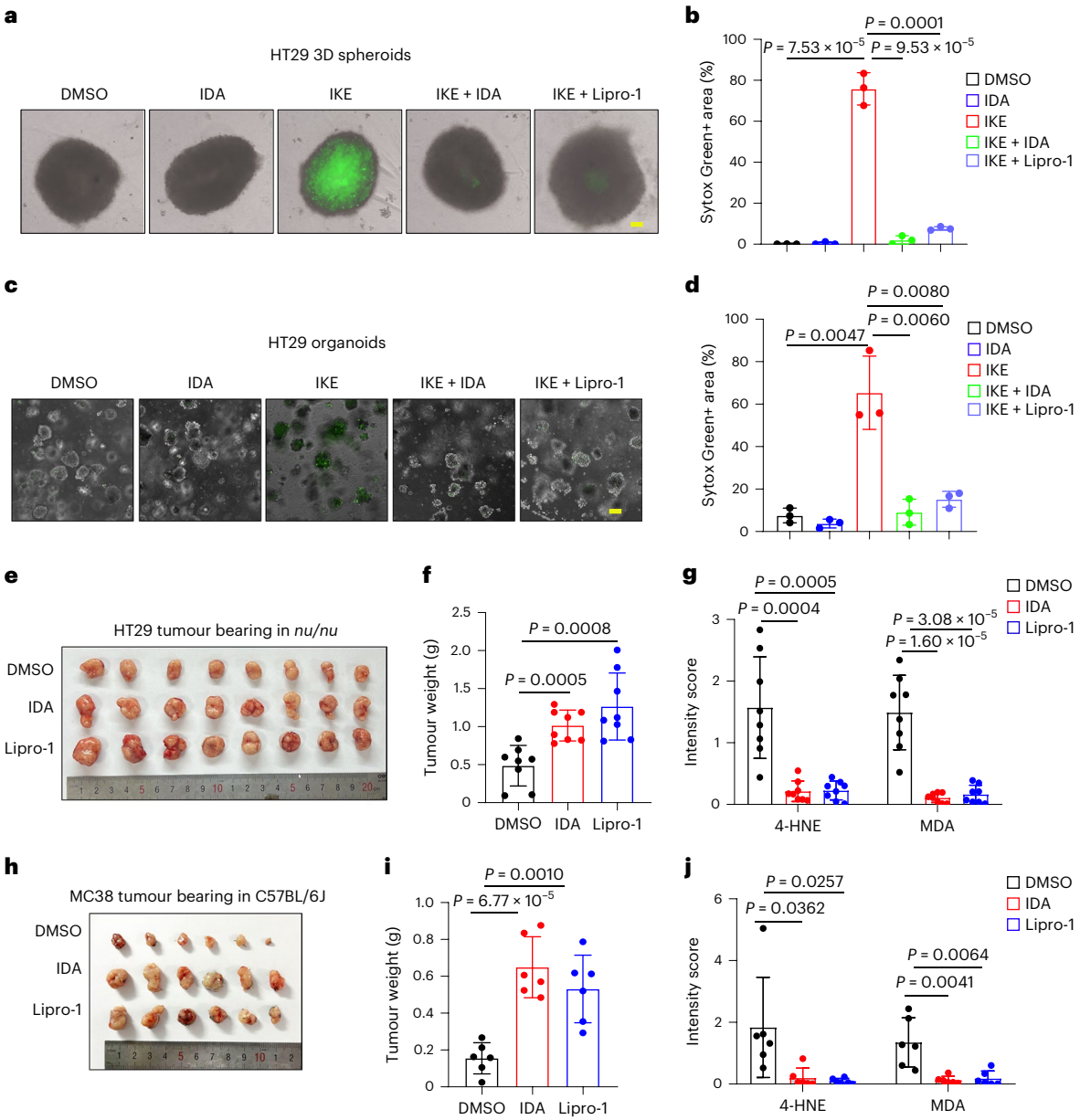

Fig. 2 | IDA facilitates colorectal tumour development. a,**b**, Representative images of HT29 3D spheroids (**a**) treated with IKE (10 μM), IDA (100 μM) and Lipro-1 (1 μM) for 48 h. Scale bars, 100 μm. **b**, Calculation of the Sytox Green-positive area. **c**,**d**, Representative images of HT29 spheroids (**c**) formed according to organoid culture protocol treated with IKE (10 μM), IDA (100 μM) and Lipro-1(1 μM) for 72 h. Scale bars, 100 μm. **d**, Calculation of the Sytox Green-positive area. **e**, Xenograft tumours of HT29 cells in *nu/nu* mice supplemented with IDA (50 mg kg^{-1}, i.p. daily) and Lipro-1 (10 mg kg^{-1}, i.p. once every 2 d) ($n = 8$ independent tumours). **f**, Analysis of tumour weight from the tumour samples in **e** ($n = 8$ independent tumours). **g**, Immunochemistry intensity scoring of 4-HNE and MDA staining in HT29 xenograft tumours ($n = 8$ independent tumours). **h**–**j**, Analysis of MC38 tumour bearing in C57BL/6J mice supplemented with (50 mg kg^{-1}, i.p. daily) and Lipro-1 (10 mg kg^{-1}, i.p. once every 2 d) (**h**) and the data of tumour weight (**i**) and intensity scoring of 4-HNE and MDA staining (**j**) ($n = 6$ independent tumours). Data and error bars are mean ± s.d., $n = 3$ biological independent experiments in **b** and **d**. All *P* values were calculated using two-tailed, unpaired Student's *t*-test.

axis might regulate ferroptosis through NRF2. To test this possibility, we first examined the levels of NRF2 and its transcriptional targets on IDA treatment. Surprisingly, no change of NRF2 and its target genes was observed (Extended Data Fig. 5b,c). To further validate this finding, we blocked the expression of NRF2 and found that deficiency of NRF2 has no effect on IDA-mediated ferroptosis (Extended Data Fig. 5d,e).

We next examined the change of classic ferroptosis-related proteins on IDA treatment. As shown in Extended Data Fig. 5f,g, supplementation of IDA did not significantly affect the status of these ferroptosis-related proteins. To further test whether GPX4 is involved in IDA-regulated ferroptosis suppression, we established GPX4$^{-/-}$ HT1080 cells (Extended Data Fig. 5h). IDA robustly protected GPX4$^{-/-}$ cells against ferroptosis on Fer-1 withdrawal (Extended Data Fig. 5i). However, deficiency of AHR in GPX4$^{-/-}$ cells abrogated the protective effect of IDA (Extended Data Fig. 5j,k). In addition, loss of DHODH or GTP cyclohydrolase 1 (GCH1) has an inability to restore ferroptosis on IDA treatment (Extended Data Fig. 5l–o).

FSP1, which catalyses the generation of reduced CoQ10 using NAD(P)H, protected cells from ferroptosis parallel to the GPX4 system

https://doi.org/10.1038/s41556-023-01314-6

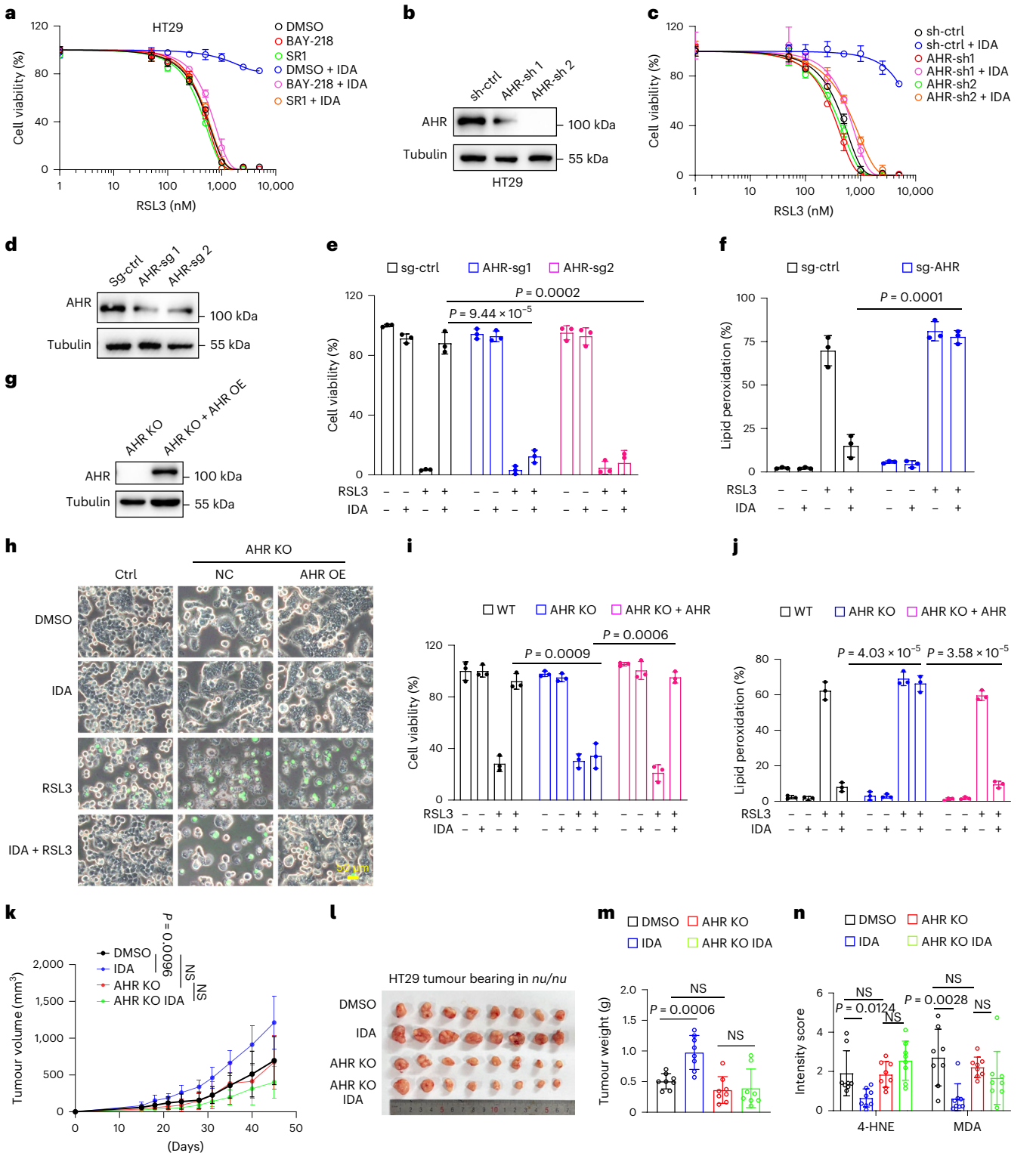

Fig. 3 | AHR is required for IDA-mediated ferroptosis inhibition. a, Cell viability in HT29 cells treated with RSL3, IDA (50 μM), BAY-218 (10 μM) and SR1 (10 μM) for 24 h. **b**, Western blotting analysis of HT29 cells expressing shRNA-ctrl or AHR-shRNA. **c**, Cell viability in HT29 cells expressing shRNA-ctrl or AHR-shRNA treated with RSL3 for 24 h with IDA treatment. **d**, Western blotting analysis of HT29 cells expressing sg-ctrl or AHR-sg. **e**,**f**, Cell viability (**e**) and lipid peroxidation (**f**) of HT29 cells expressing sg-ctrl or AHR-sg treated with RSL3 (5 μM) and IDA (50 μM) for the indicated times. **g**, Western blotting analysis of HT29 AHR KO cells with ectopic expression of AHR. **h**, Representative phase-contrast images of HT29 AHR KO cells with empty vector or ectopic expression of AHR treated with RSL3 (5 μM). Dead cells were stained with Sytox Green. Scale bars, 50 μm. **i**,**j**, Cell viability (**i**) and lipid peroxidation (**j**) of HT29 AHR KO cells with ectopic expression of AHR treated with RSL3 (5 μM) and IDA (50 μM) for the indicated times. **k**–**m**, Tumour volumes (**k**), tumour images (**l**) and weights (**m**) of HT29 WT and AHR KO xenografts in *nu/nu* mice with or without IDA supplementation (50 mg kg^{-1}, i.p.) daily ($n = 8$ independent tumours). **n**, Immunochemistry intensity scoring of 4-HNE and MDA staining in HT29 WT and AHR KO xenograft tumours with or without IDA treatment ($n = 8$ independent tumours). The western blotting experiments were repeated three times independently with similar results in **b**, **d** and **g**. NS, not significant; OE, overexpression. Data and error bars are mean ± s.d., $n = 3$ biological independent experiments in **a**, **c**, **e**, **f**, **h**, **i** and **j**. All *P* values were calculated using two-tailed, unpaired Student's *t*-test. Ctrl, control.

https://doi.org/10.1038/s41556-023-01314-6

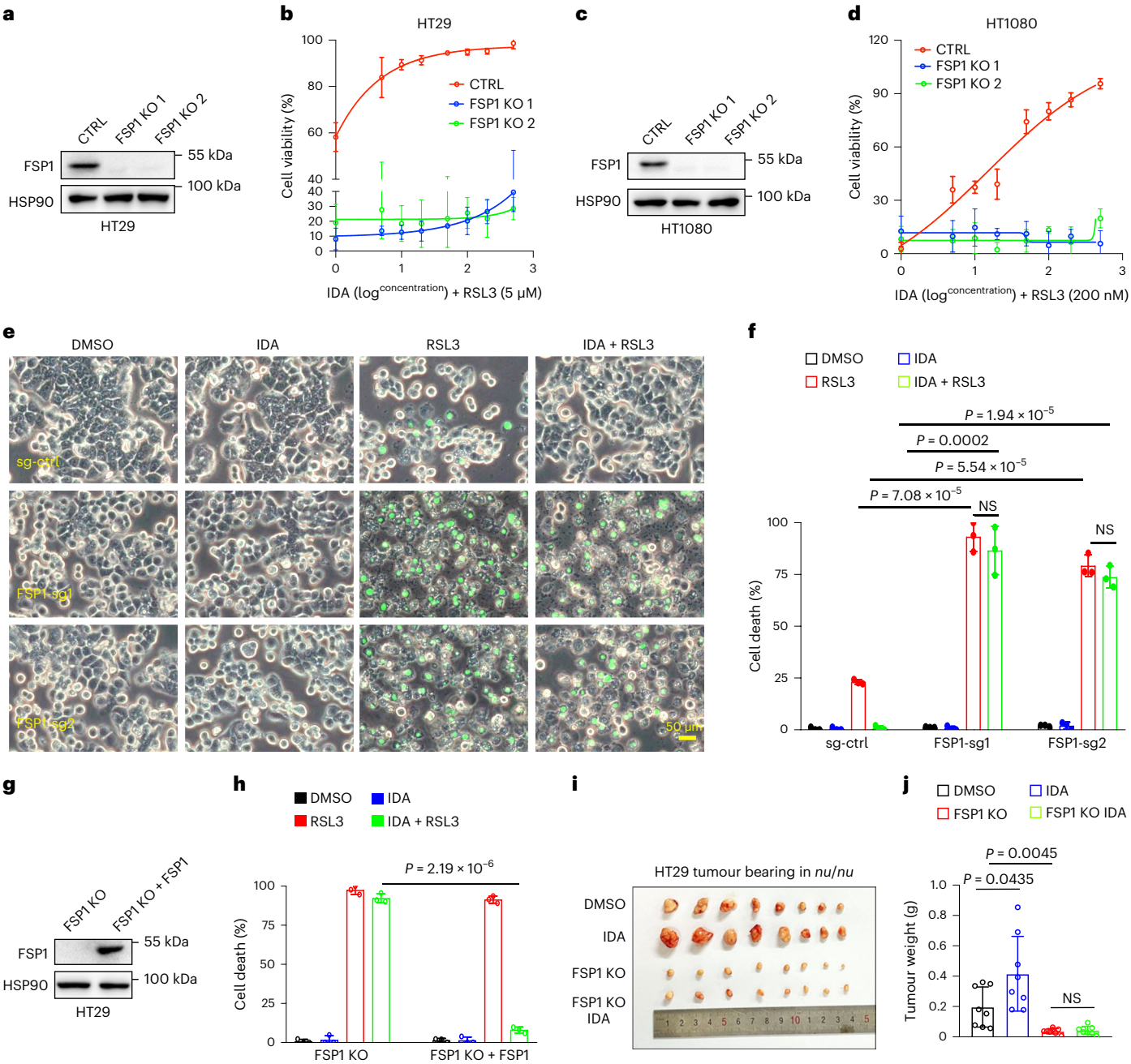

Fig. 4 | FSP1 is required for the anti-ferroptotic effect of IDA. a, Western blotting analysis of control and FSP1 KO HT29 cells. **b**, Cell viability in HT29 FSP1 KO cells treated with the indicated concentrations of IDA (5–500 μM) and RSL3 (5 μM) for 24 h. **c**, Western blotting analysis of control and FSP1 KO HT1080 cells. **d**, Cell viability in HT1080 FSP1 KO cells treated with the indicated concentrations of IDA (5–500 μM) and RSL3 (200 nM) for 12 h. **e**,**f**, Representative phase-contrast images (**e**) of HT29 cells expressing sg-ctrl or sg-FSP1 treated with RSL3 (5 μM) and IDA (50 μM). Dead cells were stained with Sytox Green (**f**). Scale bars, 50 μm. **g**, Western blotting analysis of HT29 FSP1 KO cells with ectopic expression of FSP1. **h**, Cell death of HT29 FSP1 KO cells with ectopic expression of FSP1 treated with RSL3 (5 μM) and IDA (50 μM). **i**,**j**, Tumour image (**i**) and weights (**j**) of HT29 WT and FSP1 KO xenografts in *nu/nu* mice with supplementation of IDA (50 mg kg^{-1}) daily ($n = 8$ independent tumours). The western blotting experiments were repeated three times independently with similar results in **a**, **c** and **g**. Data and error bars are mean ± s.d., $n = 3$ biological independent experiments in **b**, **d**, **f** and **h**. All *P* values were calculated using two-tailed, unpaired Student's *t*-test.

as cytoplasm membrane protein[11]. We therefore generated FSP1$^{-/-}$ clones in HT29 and HT1080 cells to validate whether FSP1 contributes to IDA-regulated ferroptosis resistance. As shown in Fig. 4a,b, KO of FSP1 in HT29 cells largely abrogated the protective effect of the IDA–AHR axis, whereas WT HT29 cells markedly responded to IDA-mediated ferroptosis suppression. Consistently, deficiency of FSP1 in HT1080 cells completely blocked the anti-ferroptotic effect of IDA similar to HT29 FSP1 single guide (sg)RNA cells (Fig. 4c–f). In contrast, ectopic expression of FSP1 rescued this phenotype (Fig. 4g,h). To better clarify that IDA-mediated ferroptosis resistance is specifically dependent on FSP1, we performed experiments in FSP1 KO and GCH1 KO cell lines. Consistent with previous studies, FSP1 KO or GCH1 KO makes cells more sensitive to ferroptosis (Extended Data Fig. 5p). We demonstrated that IDA treatment blocked ferroptosis in GCH1 KO cells, whereas there was no protective effect in FSP1 KO cells (Extended Data Fig. 5q). Vitamin K (MK4), a specific substrate of FSP1 for inhibiting ferroptosis, was

used as a positive control (Extended Data Fig. 5r)[24,25]. Phospholipids containing PUFA are the major substrates for lipid peroxidation[9,10]. Non-targeted lipidomics assay revealed that IDA did not affect the contents of phospholipids (Extended Data Fig. 6). In addition, supplementation of IDA promoted tumour development in HT29 WT cells, whereas the effect of IDA was largely abrogated in FSP1 KO cells (Figs. 4i,j), indicating that the IDA–AHR axis-mediated ferroptosis suppression is dependent on FSP1.

IDA inhibits ferroptosis via the AHR–*ALDH1A3*–FSP1–CoQ10 axis

The aforementioned findings raised the question of how FSP1 participates in IDA–AHR-mediated ferroptosis inhibition. To elucidate this question, we performed RNA sequencing (RNA-seq) for IDA-treated HT29 cells. Among the top ranked genes potentially mediated by IDA, *ALDH1A3* was the most upregulated (Fig. 5a and Supplementary Table 1). In addition, as our aforementioned data showed that IPA was incapable of ferroptosis resistance, we carried out comparative RNA-seq between IDA- and IPA-treated cells to look for candidates specifically involved in the IDA response. It is interesting that *ALDH1A3* was significantly higher in IDA- but not IPA-treated HT29 cells (Extended Data Fig. 7a,b and Supplementary Tables 2 and 3), indicating that *ALDH1A3* is specifically regulated by IDA stimulation. Furthermore, gene ontology (GO) analysis of differential genes found that the pathway of NADH dehydrogenase (quinone/ubiquinone) activity is specifically enriched in IDA-treated cells (Extended Data Fig. 7c,d), implying that the IDA–AHR axis might facilitate FSP1-regulated anti-ferroptosis via the NADH-mediated reduction of CoQ10. As *ALDH1A3* is involved in NADH generation, we therefore focused our attention on this. Reverse transcriptase quantitative PCR (RT–qPCR) and western blotting analysis confirmed that messenger RNA and protein levels of ALDH1A3 were dramatically increased on IDA treatment (Fig. 5b,c and Extended Data Fig. 7e), although there was no significant change on other tryptophan metabolite treatment (Extended Data Fig. 7f), implying that *ALDH1A3* might be a direct downstream target of AHR. Therefore, we next sought the potential AHR-binding loci surrounding the *ALDH1A3* promoter. By comparing with the consensus AHR-binding motif (GCGTG), we found three potential binding regions (R1–R3), in which R3 contains an identical sequence (Fig. 5d). A ChIP assay was performed in HT29 with or without IDA treatment. It is interesting that endogenous AHR exhibited a strong binding affinity to R3 at ~100 bp upstream of the *ALDH1A3* transcription starting site (TSS) on IDA treatment, but not to R1 or R2 (Fig. 5e), demonstrating the recruitment of AHR on the *ALDH1A3* promoter under activation of AHR by IDA.

To test the role of ALDH1A3 in ferroptosis, we blocked the expression of ALDH1A3 in HT29 cells (Extended Data Fig. 7g) and examined the levels of ferroptotic cell death. As shown in Fig. 5f,g, loss of ALDH1A3 markedly sensitized cells to lipid peroxidation-induced ferroptosis. Moreover, reduced expression of ALDH1A3 impaired the ability of IDA to inhibit ferroptosis (Fig. 5h). ALDH1A3 specifically utilizes all-*trans*-retinal as a substrate to generate NADH[26]. Supplementation of retinoic acid (RA) biosynthesis intermediates in the cells showed that retinal and vitamin A (a mixture of retinal, retinol and RA) robustly protected cells against ferroptosis; however, RA did not affect cellular sensitivity to ferroptosis (Extended Data Fig. 7h). More specifically, retinal- or vitamin A-modulated ferroptosis protection is dependent on ALDH1A3 (Fig. 5i), indicating that retinal renders cells resistant to ferroptosis via enzymatic activity of ALDH1A3. Consistently, similar phenotypes were observed in HT29 and HT1080 cells transfected with *ALDH1A3* siRNA (Extended Data Fig. 7i–o). Furthermore, ectopic expression of ALDH1A3 rescued cell death in HT29 ALDH1A3 KO cells (Extended Data Fig. 8a,b). We also used the *ALDH1* enzymatic inhibitor disulfiram to test the role of ALDH1A3. As expected, disulfiram induced high levels of ferroptotic cell death and attenuated the effect of IDA- and ALDH1A3-mediated ferroptosis inhibition (Fig. 5j and Extended Data Fig. 8c).

To investigate the role of ALDH1A3 in tumour development, we tested whether loss or pharmacological inhibition of ALDH1A3 influences tumour cell growth. As expected, loss of ALDH1A3 substantially inhibited tumour progression and blocked IDA-promoted tumour growth (Fig. 5k,l). Consistent with this finding, knockdown of ALDH1A3 in MC38 cells reversed the protective effect of IDA on tumour development (Extended Data Fig. 8d–g). Moreover, disulfiram markedly suppressed tumour growth of HT29 xenografts and the tumour growth suppression could be restored by treatment with the ferroptosis inhibitor α-tocopherol (Extended Data Fig. 8h–l). Taken together, our data support IDA–AHR pathway-mediated ferroptosis inhibition being dependent on ALDH1A3.

To further verify whether NADH generated by ALDH1A3 participates in FSP1-mediated reduced CoQ10 synthesis, we first investigated the enzymatic activity of ALDH1A3 to produce NADH. An in vitro assay demonstrated that purified ALDH1A3 could generate NADH using retinal (Fig. 5m,n). Moreover, loss of ALDH1A3 dramatically reduced NADH levels, whereas supplementation of NADH in ALDH1A3 KO cells restored ferroptotic cell death (Fig. 5o,p). Moreover, a lower ratio of reduced to oxidized CoQ10 was detected in ALDH1A3$^{-/-}$ as well as FSP1$^{-/-}$ cells (Fig. 5q). Together, these data indicate that ALDH1A3 is essential for IDA–AHR–FSP1–CoQ10-mediated ferroptosis inhibition.

P. anaerobius is a major factor for IDA biosynthesis

To investigate the source of IDA in CRC development, we isolated the microbial species from the faeces of healthy humans and patients with CRC and conducted large-scale characterizations of microbiota composition using 16S ribosomal RNA gene sequencing and mass spectrometry (MS) for metabolomics analysis, respectively. It is interesting that we found that *P. anaerobius*, a known bacterium associated with CRC[6], is markedly enriched in patients with CRC (Fig. 6a). Analysis of metabolites by MS showed that *P. anaerobius* generated a detectable content of IDA (Fig. 6b and Supplementary Table 4). Furthermore, the content of IDA in the faeces of patients with CRC is much higher

Fig. 5 | IDA inhibits ferroptosis via the AHR–*ALDH1A3*–FSP1–CoQ10 axis. **a**, Heatmaps of the 12 top genes potentially regulated on IDA (50 μM) treatment in HT29 cells. **b**, Relative mRNA levels of *ALDH1A3* on IDA (50 μM) treatment in HT29 cells. **c**, Western blotting analysis of ALDH1A3 expression followed with IDA (50 μM) treatment in HT29 cells. **d**, Schematic representation of the promoter region in the human *ALDH1A3* gene. **e**, ChIP analysis of the recruitment of AHR to the *ALDH1A3* promoter with or without IDA (50 μM) treatment. **f**, Sytox Green indicating cell death of HT29 cells expressing sg-ctrl or sg-*ALDH1A3* treated with RSL3 (5 μM) and Fer-1 (1 μM) for 8 h. **g**, Analysis of the levels of lipid peroxidation in HT29 WT and ALDH1A3 KO cells treated with RSL3 (5 μM) and Fer-1 (1 μM) for 4 h by staining with C11-BODIPY 581/591. **h**, Cell death of HT29 cells expressing sg-ctrl or ALDH1A3-sg treated with RSL3 (5 μM) and IDA (50 μM) for 8 h. **i**, Cell viability in HT29 cells expressing sg-ctrl or ALDH1A3-sg treated with RSL3, vitamin A (10 μM) or retinal (10 μM) for 24 h. **j**, Cell death of HT29 cells treated with RSL3 (5 μM), disulfiram (10 μM), IDA (50 μM) or retinal (10 μM) for 8 h. **k**,**l**, Tumour image (**k**) and weights (**l**) of HT29 WT and ALDH1A3 KO xenografts in *nu/nu* mice with supplementation of IDA (50 mg kg^{-1}) daily ($n = 6$ independent tumours). **m**, Flag-ALDH1A3 was overexpressed in HEK293T cells and purified using flag M2 beads. **n**, In vitro NADH generation using retinal as the substrate with or without supplementation of purified ALDH1A3 from (**m**). **o**, NADH levels measured by an enzymatic assay in HT29 WT and ALDH1A3 KO cells. **p**, Cell death of HT29 ALDH1A3 KO cells treated with RSL3 (5 μM) after supplementation with DMSO or NADH (10 μM). **q**, Relative ratio of reduced CoQ10 to oxidized CoQ10 in HT29 WT, ALDH1A3 KO and FSP1 KO cells. The western blotting experiments were repeated three times independently with similar results to **c**. Data and error bars are mean ± s.d., $n = 3$ biological independent experiments in **b**, **e**–**j** and **n**–**q**. All *P* values were calculated using two-tailed, unpaired Student's *t*-test.

https://doi.org/10.1038/s41556-023-01314-6

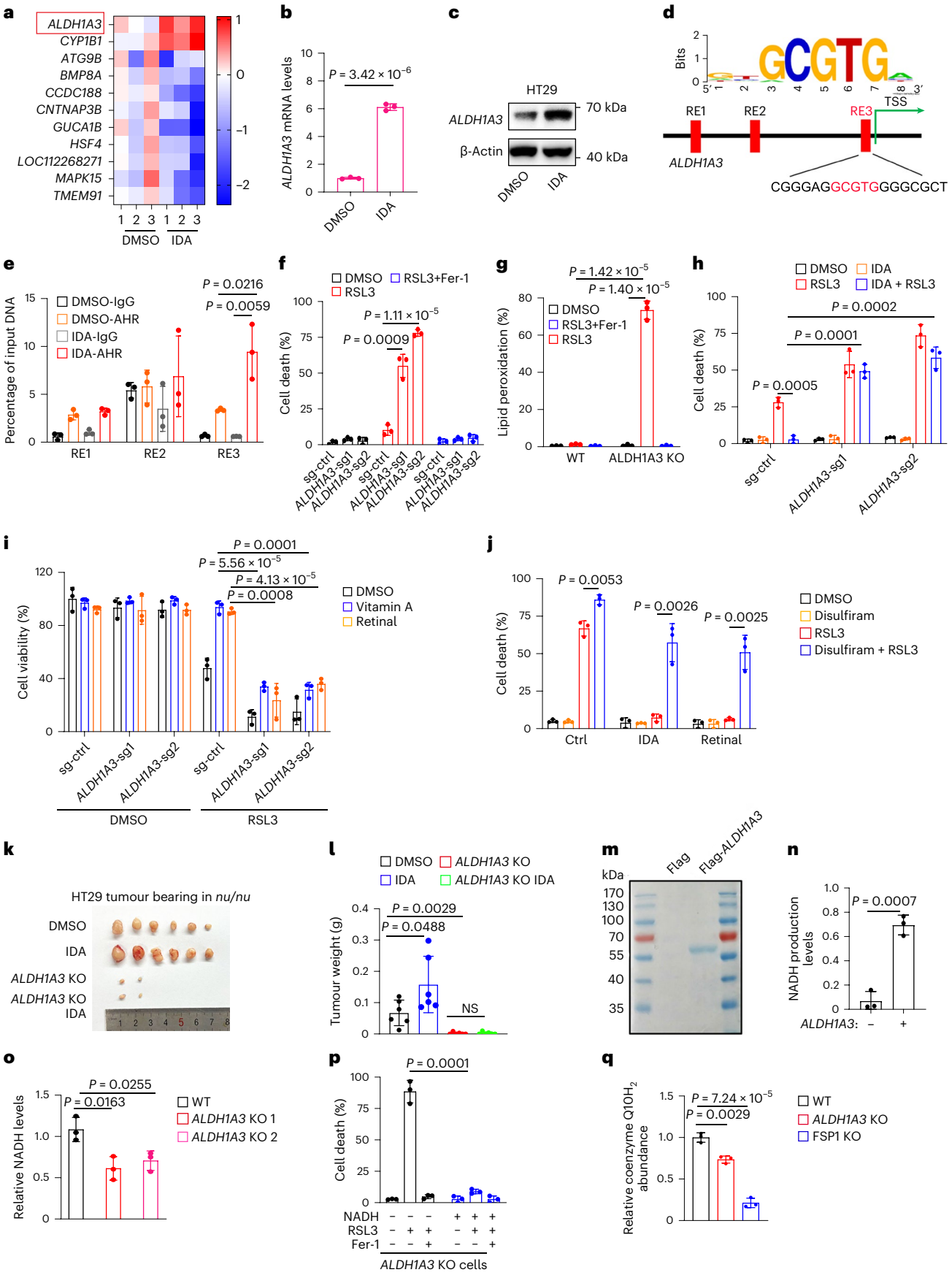

https://doi.org/10.1038/s41556-023-01314-6

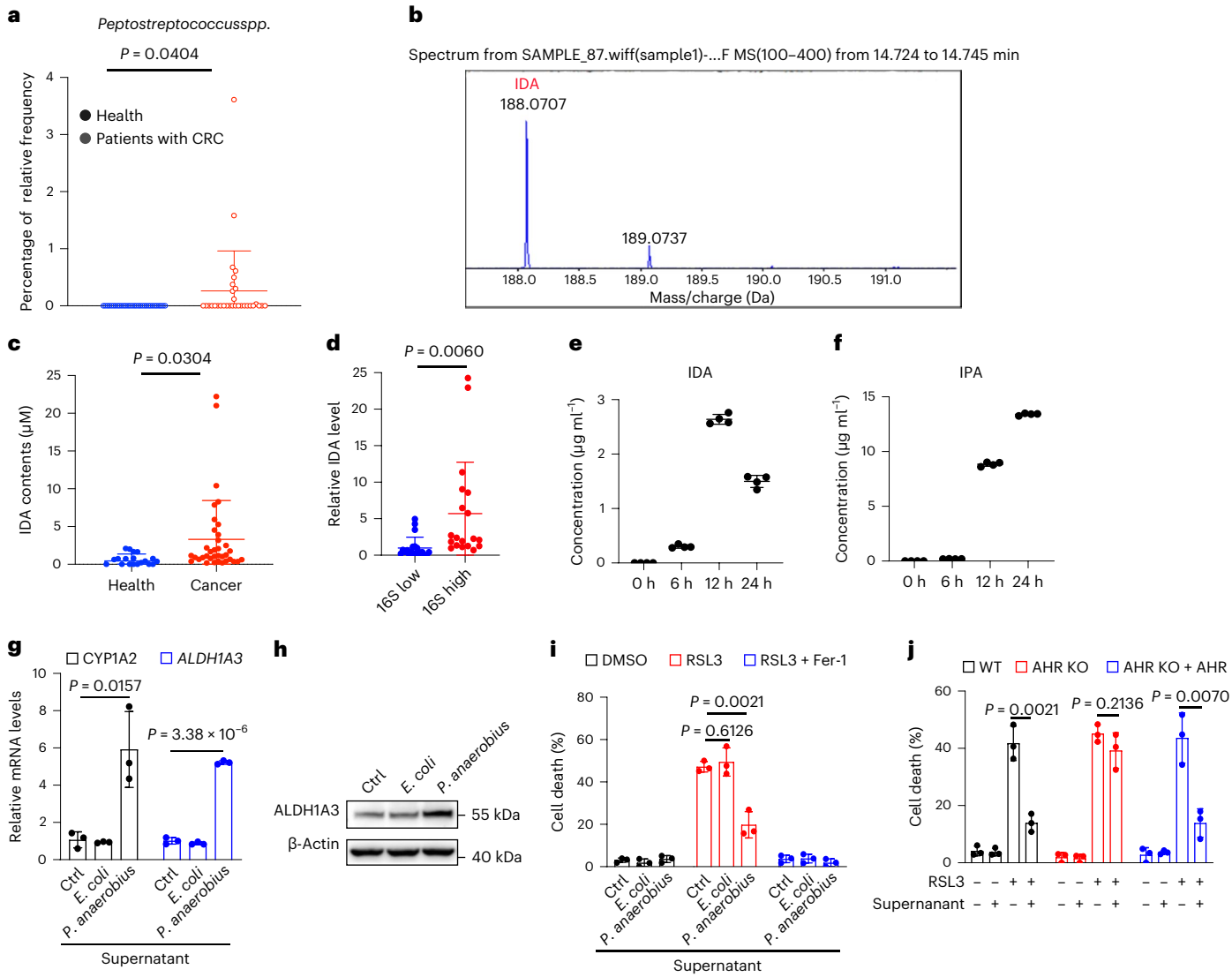

Fig. 6 | *P. anaerobius* is a major factor for IDA biosynthesis. a, Enrichment of *Peptostreptococcus* spp. in healthy humans ($n = 31$) and patients with CRC ($n = 31$) by 16S rRNA-seq technology. **b**, LC–MS analysis identifying the contents of IDA generated by *P. anaerobius* from **a**. **c**, LC–MS analysis of IDA contents in the faeces of healthy humans ($n = 19$) and patients with CRC ($n = 36$). **d**, Comparison of IDA contents in the faeces of patients with CRC with low ($n = 20$) or high ($n = 19$) abundance of *P. anaerobius*. **e**,**f**, LC–MS analysis of IDA (**e**) and IPA (**f**) contents derived from *P. anaerobius* supernatant with indicated times. **g**, Relative mRNA levels of *CYP1A2* and *ALDH1A3* in HT29 cells supplemented with supernatant from *E. coli* or *P. anaerobius*. **h**, Western blotting analysis of ALDH1A3 expression in HT29 cells supplemented with supernatant from *E. coli* or *P. anaerobius*. **i**, Cell death of HT29 cells treated with RSL3 (5 μM) for 8 h after supplementation with supernatant from *E. coli* or *P. anaerobius*. **j**, Cell death of HT29 WT, AHR KO and AHR KO + AHR cells treated with RSL3 (5 μM) for 8 h after supplementation with supernatant from *E. coli* or *P. anaerobius*. The western blotting experiments were repeated three times independently with similar results to **h**. Data and error bars are mean ± s.d., $n = 4$ (**e** and **f**) and $n = 3$ biological independent experiments in **g**, **i** and **j**. All *P* values were calculated using two-tailed, unpaired Student's *t*-test.

than in healthy humans (Fig. 6c) and the abundance of *P. anaerobius* is positively correlated with the faecal IDA levels (Fig. 6d).

In addition, we isolated the 44 bacterial species enriched in patients with CRC and examined the activation of AHR using these bacterial supernatants. (Extended Data Fig. 9a,b). Strains that significantly upregulated cytochrome P450 family 1 subfamily A member 1 (cyp1a1) and cyp1a2 were then subjected to IDA detection by LC–MS. Among all 44 strains, only *P. anaerobius* has the ability to produce IDA (Extended Data Fig. 9c). In addition, previous studies indicate that *P. russellii*, *P. stomatis*, *P. anaerobius* and *Clostridium sporogenes* are the only four species that contain the phenyl-lactate dehydratase gene clusters (fldAIBC) to generate IDA[23,27]. *P. anaerobius* generates a much higher level of IDA than *P. russellii* or *P. stomatis*[23,27]. In addition, we also analysed the relative abundance of *P. anaerobius*, *P. russellii* and *C. sporogenes* in patients with CRC from public data[28]. As shown in Extended Data Fig. 9d, the relative abundance of *P. anaerobius* significantly increased along with the disease progression, whereas the abundance of *P. russellii* and *C. sporogenes* is much lower and not enriched in patients with CRC. These data reveal that *P. anaerobius* is the major contributor of in vivo IDA biosynthesis in patients with CRC.

We cultured *P. anaerobius* under anaerobic conditions for the indicated time and used liquid chromatography (LC)–MS technology to detect the levels of a variety of tryptophan derivatives from the supernatant. Indeed, *P. anaerobius* efficiently utilized tryptophan to produce high levels of IDA and IPA (Fig. 6e,f and Extended Data Fig. 10a). Conversely, a low abundance of 3-indole, indole-3-aldehyde (IAld), indole-3-lactic acid (ILA), 3-indole and indole-3-acetic acid (IAA) was detected (Extended Data Fig. 10b–e). We observed that the

https://doi.org/10.1038/s41556-023-01314-6

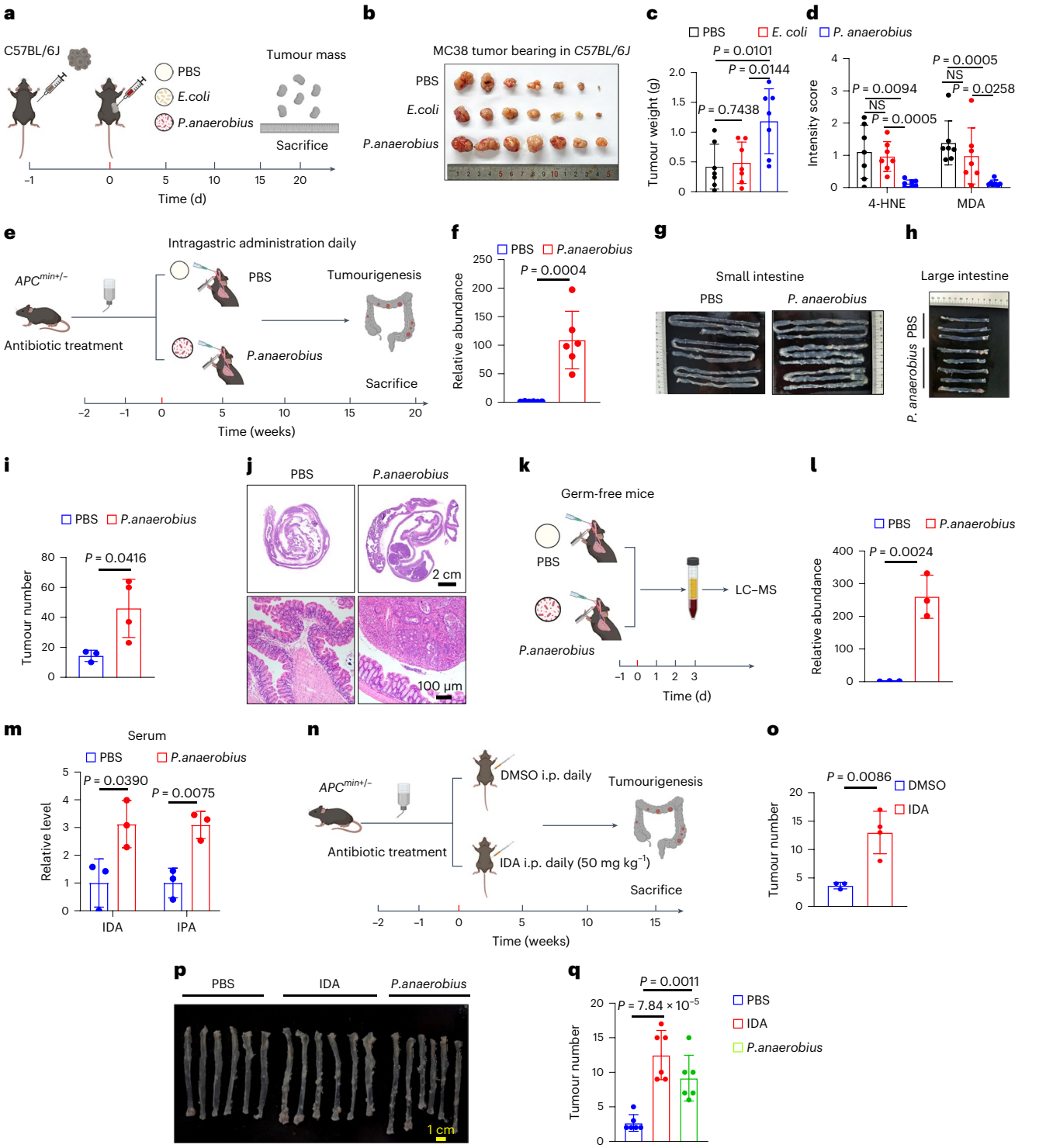

Fig. 7 | *P. anaerobius* or IDA promotes in situ CRC progression. a,**b**, Model of MC38 tumour bearing in C57BL/6J mice supplemented with PBS, *E. coli* or *P. anaerobius* (1×10^8 c.f.u.) (**a**) by intratumoural injection once every 2 d. Tumour images are shown in **b** ($n = 7$ independent tumours). **c**, Analysis of tumour weight of MC38 xenografts from **a** ($n = 7$ independent tumours). **d**, Immunochemistry intensity scoring of 4-HNE and MDA staining in the tumour samples from **a** ($n = 7$ independent tumours). **e**, Model of $Apc^{Min/+}$ mice treated with PBS or *P. anaerobius* (1×10^8 c.f.u.) via intragastric administration daily for 20 weeks, preceded by microbiota depletion with antibiotics for 2 weeks. **f**, RT–qPCR analysis of the colonization efficiency of *P. anaerobius* in the $Apc^{Min/+}$ mice treated with PBS or *P. anaerobius* ($n = 6$ independent mice). **g**,**h**, Representative images of tumourigenesis of small (**g**) and large (**h**) intestines on PBS or *P. anaerobius* treatment. **i**, Statistics of tumour numbers of small and large intestines derived from $Apc^{Min/+}$ mice treated with PBS or *P. anaerobius* (PBS, $n = 3$ and *P. anaerobius*, $n = 4$ independent mice). **j**, Representative images of tumourigenesis of large intestines visualized by H&E staining. **k**–**m**, Model of germ-free mice (**k**) treated with PBS or *P. anaerobius* intragastric administration, colonization efficiency of *P. anaerobius* (**l**) and IDA contents (**m**) in plasma analysed after 3 d ($n = 3$ independent mice). **n**, Model of $Apc^{Min/+}$ mice treated with IDA (50 mg kg^{-1}) injected i.p. for 15 weeks, followed by microbiota depletion with antibiotics for 2 weeks. **o**, Statistics of tumour numbers of intestines from **n** ($n = 3$ independent mice). **p**,**q**, Representative images of tumourigenesis of large intestines (**p**) on IDA (i.p. 50 mg kg^{-1}) and *P. anaerobius* treatment in the AOM/DSS model of colitis-associated cancer ($n = 6$ independent mice). Tumour numbers are shown in **q**. Data and error bars are mean ± s.d. All *P* values were calculated using two-tailed, unpaired Student's *t*-test.

https://doi.org/10.1038/s41556-023-01314-6

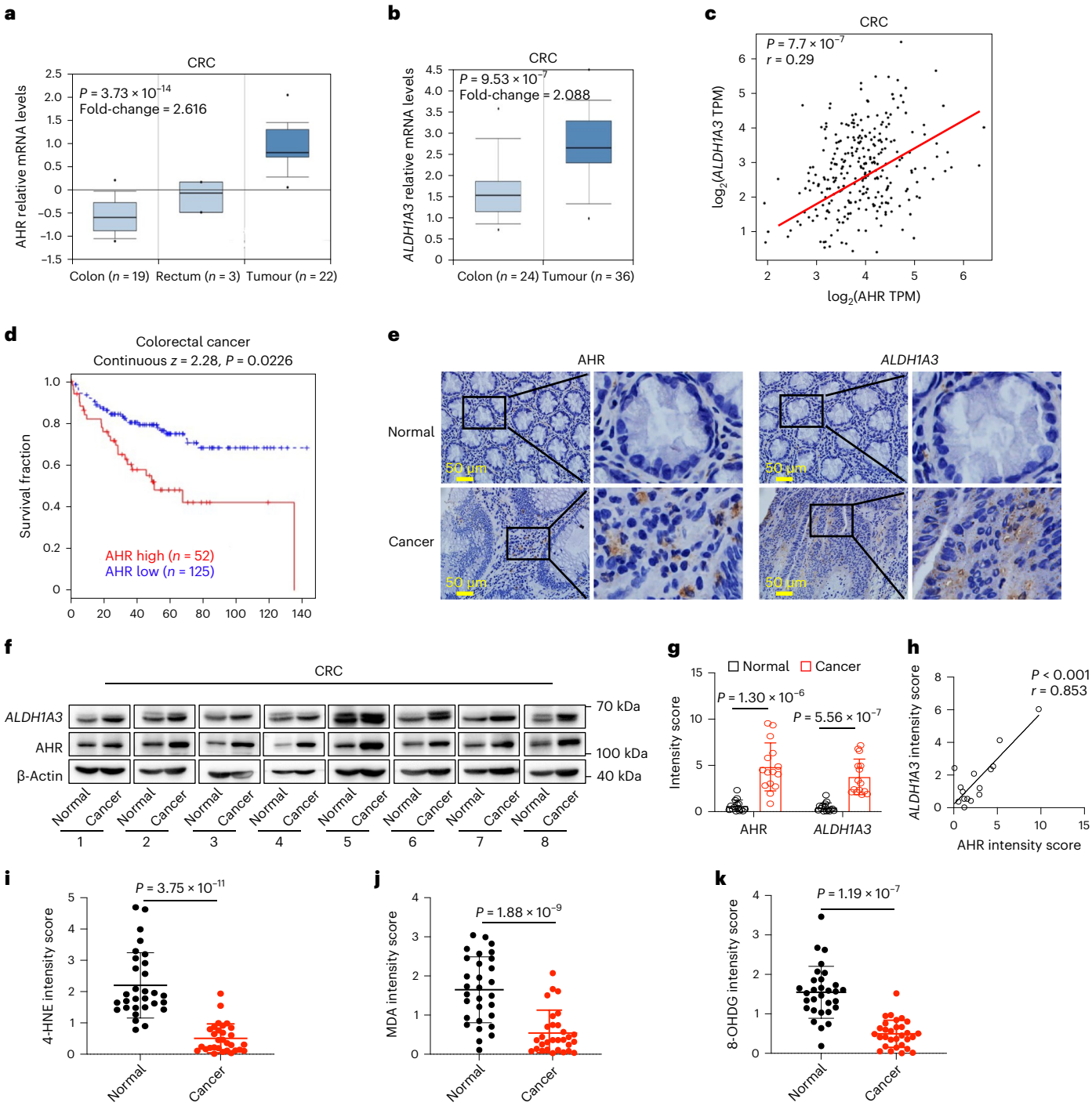

Fig. 8 | The AHR–*ALDH1A3* pathway is negatively correlated with prognosis in patients with CRC. a,**b**, Oncomine database analysis of mRNA levels of AHR (**a**) and *ALDH1A3* (**b**) in patients with CRC (https://www.oncomine.org) (colon, $n = 19$, rectum, $n = 3$ and tumour, $n = 22$ in **a** and colon, $n = 24$ and tumour, $n = 36$ in **b**). Box plots show the centre line at median and the box limits at the 25th/75th percentiles. **c**, Dot plot showing the correlation of the expression level of AHR and *ALDH1A3* in the colorectal tumour samples from the TCGA dataset. **d**, Kaplan–Meier survival curves for patients with the indicated types of cancers containing low or high expression of AHR mRNA in the TCGA dataset. The *P* value was calculated using the log(rank Mantel–Cox test). **e**, IHC staining of AHR and *ALDH1A3* in the samples from the patients with CRC. Scale bars, 50 μm. **f**, Western blotting analysis of AHR and *ALDH1A3* in human CRC samples ($n = 8$). **g**, Intensity scores of AHR and *ALDH1A3* in human CRC samples ($n = 15$). The intensity of AHR and *ALDH1A3* was scored. **h**, Dot plot showing the correlation of the expression level of AHR and *ALDH1A3* in the colorectal tumour samples from **g**. **i**–**k**, Immunochemistry scoring of 4-HNE (**i**), MDA (**j**) and 8-OHDG (**k**) staining in the human colorectal samples ($n = 30$ independent samples). The western blotting experiments were repeated three times independently with similar results to **f**. The *P* values (**g** and **i**–**k**) were calculated using two-tailed, unpaired Student's *t*-test. The bivariate relationship (**c** and **h**) was calculated using Spearman's rank correlation coefficient.

concentration of IDA reached about 15 μM at 12 h (Fig. 6e). Moreover, the level of *ALDH1A3* as well as *CYP1A2* was greatly increased in HT29 cells on treatment of *P. anaerobius* supernatant, whereas there was no effect of the supernatant of *Escherichia coli* (Fig. 6g,h). Moreover, ferroptosis was markedly suppressed in the cells supplemented with the supernatant of *P. anaerobius* (Fig. 6i). As expected, loss of

AHR abrogated the effect and overexpression of AHR rescued the protective effect (Fig. 6j). In addition, HT29 cells cocultured with *P. anaerobius* exhibited upregulation of *ALDH1A3* and resistance to ferroptosis (Extended Data Fig. 10f,g). In accordance with this, we observed a consistent phenomenon in MC38 cells (Extended Data Fig. 10h–l).

A previous study has shown that *P. anaerobius* specifically adheres to the CRC mucosa and the direct interaction between *P. anaerobius* and CRC cells makes it possible to generate a sufficient concentration of IDA to suppress CRC ferroptosis[6]. To further demonstrate whether the physiological concentration of IDA in vivo defends against ferroptosis and promotes tumour progression, we first performed in vivo intratumoral injection of *P. anaerobius* and detected the content of IDA in the tumour. The concentration of IDA in the tumour (about 5 μM; Extended Data Fig. 10m) efficiently decreased CRC ferroptosis and facilitated tumour growth (Fig. 7a–d). In addition, the physiological concentration of IDA is sufficient to abolish lipid peroxidation and ferroptosis in vivo (Figs. 7a–d). Taken together, our data demonstrated that the physiological concentration of IDA efficiently inhibits ferroptosis both in vitro and in vivo.

P. anaerobius or IDA promotes in situ CRC progression

To better mimic the in vivo gut microbiota-driven tumourigenesis, we extended our findings by adopting the *Apc* mutation ($Apc^{Min/+}$)-driven CRC model, a genetic mouse model of spontaneous CRC. As shown in Fig. 7e, *P. anaerobius* exhibited efficient colonization in colonic tissues (Fig. 7f). Moreover, *P. anaerobius*-treated $Apc^{Min/+}$ mice developed higher tumour multiplicities (Fig. 7g–j), indicating that *P. anaerobius* accelerates colorectal development in $Apc^{Min/+}$ mice.

We further explored whether *P. anaerobius*-mediated CRC development depends on IDA. For this purpose, germ-free mice, a powerful tool to better investigate the features of gut microbes, were gavaged with *P. anaerobius*. After 72 h, these mice were euthanized to detect the serum abundance of tryptophan metabolites (Fig. 7k). Consistent with the in vitro findings, IDA and IPA were significantly increased on supplementation of *P. anaerobius* (Fig. 7l,m), demonstrating that *P. anaerobius* is responsible for biosynthesis of IDA in vivo. We next evaluate whether supplementation of IDA drives colorectal tumourigenesis in $Apc^{Min/+}$ mice (Fig. 7n). As expected, IDA-treated $Apc^{Min/+}$ mice displayed remarkably higher tumour multiplicities (Fig. 7o). Furthermore, the azoxymethane/dextran sulfate sodium (AOM/DSS) model of colitis-associated cancer was established and found that IDA and *P. anaerobius* significantly promoted the progress of colitis-induced CRC (Fig. 7p,q). We also examined whether IDA might impact the functional states of tumour-infiltrating T cells in AOM/DSS-induced, orthotopic, colitis-associated cancer. As shown in Extended Data Fig. 10o, IDA cannot affect infiltrating $CD4^+$ T and $CD8^+$ T cells and neutrophils in the tumour microenvironment. However, IDA significantly upregulates the number of macrophages. In addition, we also examined these markers in the MC38 tumour-bearing model in the immunocompetent C57BL/6J mice. Although this model does not rigorously model the CRC milieu, it also exhibited a consistent phenomenon with the AOM/DSS-induced orthotopic CRC model (Extended Data Fig. 10p).

We next analysed the functional consequence of AHR in clinical samples and found that AHR and *ALDH1A3* expression is upregulated in colorectal cancers (Fig. 8a–c). Furthermore, high expression of AHR is positively correlated with poor clinical outcome in patients with CRC (Fig. 8d). Consistently, immunohistochemistry (IHC) and western blotting analysis showed that AHR and *ALDH1A3* are more highly expressed in human CRC samples (Fig. 8e–h). Moreover, IHC staining with 4-hydroxy-2-nonenal (4-HNE), 3,4-methylenedioxyamphetamine (MDA) and 8-hydroxy-2′-deoxyguanosine (8-OHDG) revealed that lower levels of lipid peroxidation were observed in colorectal cancers (Fig. 8i–k). Together, our study implies that the IDA–AHR–*ALDH1A3*–FSP1 pathway facilitates CRC development through ferroptosis inhibition.

Discussion

Emerging evidence indicates that gut microbes participate in the progression of tumorigenesis through the generation of carcinogenic microbial metabolites. However, a major issue in clinic needs to be urgently addressed: whether blocking the interaction of gut microbiota metabolites with host tissue cells abrogates tumour development.

In the present study, we revealed that a bacterial derivative of tryptophan, IDA, promoted CRC progression through ferroptosis inhibition. We identified that IDA exhibited a distinct effect in regulating ferroptosis and CRC progression compared with other indoles. AHR has been thought to play a pivotal role as an intracellular receptor for indoles. However, a most recent piece of research revealed that IAA promotes chemotherapy efficacy in pancreatic cancer independent of AHR signalling[29], arguing against the role of AHR in mediating the activity of indoles. In addition, a recent piece of research revealed that IDA, but not IPA, promoted the expression of the AHR target gene *CYP1A1* (ref. 23). Consistent with these findings, our work clarified that supplementation of other indoles does not significantly activate AHR. These data indicate that AHR has a biased preference for IDA. Moreover, different AHR ligands exhibit a distinct effect by activating AHR[30–35], indicating that AHR ligands might activate a distinct downstream pathway of AHR as a result of different conformational changes on AHR–ligand interactions.

Previous studies show that certain indole derivatives generated from plants or human tryptophan metabolism inhibit ferroptosis[36,37]. Indole-3-carbinol derived from plants acts as a ferroptosis suppressor by directly scavenging lipid peroxyl radicals[36]. In our work, we demonstrate that IDA-mediated ferroptosis inhibition is independent of RTA activity. Indole-3-pyruvate, generated from human interleukin (IL)-4-involved tryptophan metabolism, protects cells from ferroptosis by activating the NRF2 pathway[37], whereas IDA suppresses ferroptotic cell death independent of the NRF2 pathway.

Specifically, our work shows that IDA acts as an endogenous ligand of AHR to transcriptionally upregulate the expression of *ALDH1A3*, which generates NADH for FSP1-mediated synthesis of reduced CoQ10. Deficiency of AHR or *ALDH1A3* in CRC cells greatly abrogates IDA-promoted tumour development. A previous study reveals that whole-body KO of AHR in $Apc^{Min/+}$ mice induces increased caecal tumours[38]. However, a most recent piece of research demonstrates that *APC* deficiency in $Apc^{Min/+}$ mice promotes transcription factor 4/β-catenin-mediated transcriptional upregulation of tryptophan 2,3-dioxygenase 2, in turn activating the kynurenine–AHR pathway to facilitate tumour development[39], implying a context-specific role of AHR in tumour development. Three of the most recently published pieces of research showed that tryptophan metabolites derived from bacteria suppress tumour progression[29,40,41]. In sharp contrast, our study shows that another tryptophan metabolite, IDA, promotes tumour development via ferroptosis inhibition, at physiological concentrations. Thus, our study is of great significance for understanding the role of different tryptophan metabolites in tumour progression.

Online content

Any methods, additional references, Nature Portfolio reporting summaries, source data, extended data, supplementary information, acknowledgements, peer review information; details of author contributions and competing interests; and statements of data and code availability are available at https://doi.org/10.1038/s41556-023-01314-6.

References

1. Fan, Y. & Pedersen, O. Gut microbiota in human metabolic health and disease. *Nat. Rev. Microbiol.* **19**, 55–71 (2021).
2. Blander, J. M., Longman, R. S., Iliev, I. D., Sonnenberg, G. F. & Artis, D. Regulation of inflammation by microbiota interactions with the host. *Nat. Immunol.* **18**, 851–860 (2017).

3. Roy, S. & Trinchieri, G. Microbiota: a key orchestrator of cancer therapy. *Nat. Rev. Cancer* **17**, 271–285 (2017).
4. Tilg, H., Zmora, N., Adolph, T. E. & Elinav, E. The intestinal microbiota fuelling metabolic inflammation. *Nat. Rev. Immunol.* **20**, 40–54 (2020).
5. He, Y. et al. Gut microbial metabolites facilitate anticancer therapy efficacy by modulating cytotoxic $CD8^+$ T cell immunity. *Cell Metab.* **33**, 988–1000.e1007 (2021).
6. Long, X. et al. *Peptostreptococcus anaerobius* promotes colorectal carcinogenesis and modulates tumour immunity. *Nat. Microbiol.* **4**, 2319–2330 (2019).
7. Louis, P., Hold, G. L. & Flint, H. J. The gut microbiota, bacterial metabolites and colorectal cancer. *Nat. Rev. Microbiol.* **12**, 661–672 (2014).
8. Dixon, S. J. et al. Ferroptosis: an iron-dependent form of nonapoptotic cell death. *Cell* **149**, 1060–1072 (2012).
9. Doll, S. et al. ACSL4 dictates ferroptosis sensitivity by shaping cellular lipid composition. *Nat. Chem. Biol.* **13**, 91–98 (2017).
10. Kagan, V. E. et al. Oxidized arachidonic and adrenic PEs navigate cells to ferroptosis. *Nat. Chem. Biol.* **13**, 81–90 (2017).
11. Yang, W. S. et al. Regulation of ferroptotic cancer cell death by GPX4. *Cell* **156**, 317–331 (2014).
12. Bersuker, K. et al. The CoQ oxidoreductase FSP1 acts parallel to GPX4 to inhibit ferroptosis. *Nature* **575**, 688–692 (2019).
13. Doll, S. et al. FSP1 is a glutathione-independent ferroptosis suppressor. *Nature* **575**, 693–698 (2019).
14. Mao, C. et al. DHODH-mediated ferroptosis defence is a targetable vulnerability in cancer. *Nature* **593**, 586–590 (2021).
15. Soula, M. et al. Metabolic determinants of cancer cell sensitivity to canonical ferroptosis inducers. *Nat. Chem. Biol.* **16**, 1351–1360 (2020).
16. Chu, B. et al. ALOX12 is required for p53-mediated tumour suppression through a distinct ferroptosis pathway. *Nat. Cell Biol.* **21**, 579–591 (2019).
17. Jiang, L. et al. Ferroptosis as a p53-mediated activity during tumour suppression. *Nature* **520**, 57–62 (2015).
18. Wang, W. et al. $CD8^+$ T cells regulate tumour ferroptosis during cancer immunotherapy. *Nature* **569**, 270–274 (2019).
19. Zhang, Y. et al. BAP1 links metabolic regulation of ferroptosis to tumour suppression. *Nat. Cell Biol.* **20**, 1181–1192 (2018).
20. Cui, W., Liu, D., Gu, W. & Chu, B. Peroxisome-driven ether-linked phospholipids biosynthesis is essential for ferroptosis. *Cell Death Differ.* **28**, 2536–2551 (2021).
21. Fiore, A. et al. Kynurenine importation by SLC7A11 propagates anti-ferroptotic signaling. *Mol. Cell* **82**, 920–932.e927 (2022).
22. Heath-Pagliuso, S. et al. Activation of the Ah receptor by tryptophan and tryptophan metabolites. *Biochemistry* **37**, 11508–11515 (1998).
23. Wlodarska, M. et al. Indoleacrylic acid produced by commensal *Peptostreptococcus* species suppresses inflammation. *Cell Host Microbe* **22**, 25–37.e26 (2017).
24. Mishima, E. et al. A non-canonical vitamin K cycle is a potent ferroptosis suppressor. *Nature* **608**, 778–783 (2022).
25. Jin, D. Y. et al. A genome-wide CRISPR–Cas9 knockout screen identifies FSP1 as the warfarin-resistant vitamin K reductase. *Nat. Commun.* **14**, 828 (2023).
26. Duan, J. J., Cai, J., Guo, Y. F., Bian, X. W. & Yu, S. C. ALDH1A3, a metabolic target for cancer diagnosis and therapy. *Int. J. Cancer* **139**, 965–975 (2016).
27. Dodd, D. et al. A gut bacterial pathway metabolizes aromatic amino acids into nine circulating metabolites. *Nature* **551**, 648–652 (2017).
28. Yachida, S. et al. Metagenomic and metabolomic analyses reveal distinct stage-specific phenotypes of the gut microbiota in colorectal cancer. *Nat. Med.* **25**, 968–976 (2019).
29. Tintelnot, J. et al. Microbiota-derived 3-IAA influences chemotherapy efficacy in pancreatic cancer. *Nature* **615**, 168–174 (2023).
30. Apetoh, L. et al. The aryl hydrocarbon receptor interacts with c-Maf to promote the differentiation of type 1 regulatory T cells induced by IL-27. *Nat. Immunol.* **11**, 854–861 (2010).
31. Ehrlich, A. K. et al. AhR activation increases IL-2 production by alloreactive $CD4^+$ T cells initiating the differentiation of mucosal-homing $Tim3^+$ $Lag3^+$ Tr1 cells. *Eur. J. Immunol.* **47**, 1989–2001 (2017).
32. Quintana, F. J. et al. Control of T_{reg} and T_H17 cell differentiation by the aryl hydrocarbon receptor. *Nature* **453**, 65–71 (2008).
33. Schulz, V. J. et al. Non-dioxin-like AhR ligands in a mouse peanut allergy model. *Toxicol. Sci.* **128**, 92–102 (2012).
34. Singh, N. P. et al. Dietary indoles suppress delayed-type hypersensitivity by inducing a switch from proinflammatory Th17 cells to anti-inflammatory regulatory T cells through regulation of microRNA. *J. Immunol.* **196**, 1108–1122 (2016).
35. Veldhoen, M. et al. The aryl hydrocarbon receptor links T_H17-cell-mediated autoimmunity to environmental toxins. *Nature* **453**, 106–109 (2008).
36. Mishima, E. et al. Drugs repurposed as antiferroptosis agents suppress organ damage, Including AKI, by functioning as lipid peroxyl radical scavengers. *J. Am. Soc. Nephrol.* **31**, 280–296 (2020).
37. Zeitler, L. et al. Anti-ferroptotic mechanism of IL4i1-mediated amino acid metabolism. *eLife* **10**, e64806 (2021).
38. Kawajiri, K. et al. Aryl hydrocarbon receptor suppresses intestinal carcinogenesis in $Apc^{Min/+}$ mice with natural ligands. *Proc. Natl Acad. Sci. USA* **106**, 13481–13486 (2009).
39. Lee, R. et al. Synthetic essentiality of tryptophan 2,3-dioxygenase 2 in APC-mutated colorectal cancer. *Cancer Discov.* **12**, 1702–1717 (2022).
40. Bender, M. J. et al. Dietary tryptophan metabolite released by intratumoral *Lactobacillus reuteri* facilitates immune checkpoint inhibitor treatment. *Cell* **186**, 1846–1862.e1826 (2023).
41. Zhang, Q. et al. *Lactobacillus plantarum*-derived indole-3-lactic acid ameliorates colorectal tumorigenesis via epigenetic regulation of $CD8^+$ T cell immunity. *Cell Metab.* **35**, 943–960.e949 (2023).

[1]Department of Cell Biology, School of Basic Medical Sciences, Cheeloo College of Medicine, Shandong University, Jinan, China. [2]Center for Advanced Interdisciplinary Science and Biomedicine of IHM, Division of Life Sciences and Medicine, University of Science and Technology of China, Hefei, China. [3]State Key Laboratory of Microbial Metabolism, Joint International Research Laboratory of Metabolic and Developmental Sciences, Sheng Yushou Center of Cell Biology and Immunology, School of Life Sciences and Biotechnology, Shanghai Jiao Tong University, Shanghai, China. [4]State Key Laboratory of Digital Medical Engineering, Department of Otolaryngology Head and Neck Surgery, Zhongda Hospital, School of Life Sciences and Technology, Advanced Institute for Life and Health, Jiangsu Province High-Tech Key Laboratory for Bio-Medical Research, Southeast University, Nanjing, China. [5]Department of Clinical Laboratory, The Second Hospital of Shandong University, Jinan, China. [6]Qilu hospital of Shandong University, Jinan, China. [7]Institute for Cancer Research, Shenzhen Bay Laboratory, Shenzhen, China. [8]Institute for Cancer Genetics, and Department of Pathology and Cell Biology, and Herbert Irving Comprehensive Cancer Center, College of Physicians & Surgeons, Columbia University, New York, NY, USA. [9]Co-Innovation Center of Neuroregeneration, Nantong University, Nantong, China. [10]School of Life Science, Beijing Institute of Technology, Beijing, China. [11]Department of Otolaryngology Head and Neck Surgery, Sichuan Provincial People's Hospital, University of Electronic Science and Technology of China, Chengdu, China. [12]Hefei National Laboratory for Physical Sciences at Microscale, School of Basic Medical Sciences, Division of Life Sciences and Medicine, University of Science and Technology of China, Hefei, China. [13]These authors contributed equally: Weiwei Cui, Meng Guo, Dong Liu.
✉e-mail: wg8@cumc.columbia.edu; renjiec@seu.edu.cn; zhushu@ustc.edu.cn; chubo123@sdu.edu.cn

Methods

The study with mice is compliant with all relevant ethical regulations for animal experiments. All the experimental protocols were approved by the Institutional Animal Care and Use Committee of Shandong University and University of Science and Technology of China (USTC). The study for human cancer samples complied with the ethical requirements of Shandong University and USTC.

Cell culture and stable cell lines

HT29, MC38, HEK293T, HT1080 and 786-O cancer cell lines were acquired from the Cell Banks of Type Culture Collection of the Chinese Academy of Sciences and have been proved to be negative for *Mycoplasma* contamination. No cell lines used in this work were listed in the International Cell Line Authentication Committee (ICLAC) database. All cells were grown in Dulbecco's modified Eagle's medium supplemented with 10% fetal bovine serum (Biological Industries), 100 U ml^{-1} of penicillin and 100 μg ml^{-1} of streptomycin in a 37 °C incubator with 5% CO_2 humidified atmosphere.

Bacterial isolation, culture and identification

The faecal sample used for bacterial isolation was collected from a 74-year-old man with untreated primary colon cancer at stage IIIC in the First Affiliated Hospital of USTC. Healthy controls were individuals with no active infection or gastrointestinal disease in the Physical Examination Center of the First Affiliated Hospital of USTC (donor 1 is a 35-year-old woman and donor 2 a 26-year-old man). To isolate *Peptostreptococcus* strains from patients with CRC, fresh patient faecal samples were suspended in an equal volume (w/v) of phosphate-buffered saline (PBS), then serially diluted to 10^{-3} to 10^{-6}, and seeded on to 5% sheep blood-enriched Columbia agar. After culture under anaerobic conditions (85% N_2, 10% H_2 and 5% CO_2) at 37 °C for 48 h, single colonies were picked and cultivated in Gifu Anaerobic Medium (GAM) broth. Then, 36 h after liquid culture, 500 μl of bacterial liquid was suspended in an equal volume (v/v) of PBS containing 20% glycerol and stored at −80 °C until use. To isolate bacterial supernatant, the remaining bacterial liquid was centrifugation at 12,000*g* for 10 min and stored at −40 °C until use. To identify bacterial species, full-length 16S rRNA PCR was performed followed by standard Sanger sequencing; the 16S rRNA gene region was amplified with universal primers (27 forward (F): 5′-AGRGTTTGATYMTGGCTCAG-3′; 1,492 reverse (R): 5′-GGYTACCTTGTTACGACTT-3′). Bacteria were identified using BLAST.

Western blotting and antibodies

Western blotting was performed with procedures similar to those described previously. The human primary antibodies against AHR (1:1,000; Cell Signaling Technology, catalogue no. 83200), *ALDH1A3* (1:1,000, Proteintech, catalogue no. 25167-1-AP), NRF2 (1:1,000; Proteintech, catalogue no. 16936-1-AP), GPX4 (1:1000; Abcam, catalogue no. ab125066), xCT/SLC7A11 (1:1,000; Cell Signaling Technology, catalogue no. 12691), Flag-M2 (1:1,000; Sigma-Aldrich, catalogue no. F1804), Myc-Tag (1:1,000, Cell Signaling Technology, catalogue no. 2276S), NQO1 (1:1,000; Proteintech, catalogue no. 11451-1-AP), DHODH (1:1,000; Proteintech, catalogue no. 14877-1-AP), GCH1 (1:1,000; Proteintech, catalogue no. 28501-1-AP), FSP (1:1,000; Proteintech, catalogue no. 20886-1-AP), glyceraldehyde 3-phosphate dehydrogenase (1:2,000; Santa Cruz Biotechnology, catalogue no. sc-47724), β-actin (1:3,000; Proteintech, catalogue no. 66009-1-AP), HSP90 (1:3,000; ZSGB-BIO, catalogue no. TA-12) and tubulin (1:3,000; ZSGB-BIO, catalogue no TA347064) were incubated overnight at 4 °C. Sequentially, the peroxidase-conjugated goat anti-rabbit or mouse immunoglobulin G(H + L) secondary antibody (1:5,000; Jackson ImmunoResearch Laboratories, catalogue nos. 111-035-003 and 115-035-003) and enhanced chemiluminescence solution (GE Healthcare) were used for visualizing protein expression.

Cell viability, cell death and flow cytometry assay

The assays were performed with procedures similar to those described previously[42]. Sytox Green-positive cells were calculated using an inverted fluorescence microscope (Olympus). A Becton Dickinson FACS Calibur machine was used to collect the flow cytometry data.

DPPH assay

For examining whether IDA acts as an RTA to inhibit ferroptosis, DPPH assay was performed with procedures similar to those described previously[42]. Different concentrations of IDA were tested and Liprostatin-1 was used as a positive control.

FENIX assay

Egg PC liposomes (extruded to 100 nm, 1 mM), STY-BODIPY (1 μM) and an indicated concentration of IDA or vehicle (dimethyl sulfoxide (DMSO)) were vortexed in PBS (10 mM, pH 7.4), then 200-μl aliquots were incubated in a 96-well plate (poly(propylene); Nunc) for 20 min at 37 °C. Thereafter, DTUN (200 mM in EtOH) was added to the aliquots. The plate was vigorously mixed for 5 min and kinetic data of STY-$BODIPY_{OX}$ were acquired at 488 nm and 518 nm using a Mithras LB940 microplate reader (Berthold Technologies).

Generation of 3D spheroids by centrifugation

Spheroids were generated by plating 5,000–10,000 tumour cells per well into U-bottomed, ultra-low adherence, 96-well plates (Corning). Optimal 3D structures were achieved by centrifugation at 600*g* for 5 min followed by addition of 2.5% (v/v) Matrigel (Corning). Plates were incubated for 72 h at 37 °C, 5% CO_2 and 95% humidity for formation of a single spheroid of cells. Spheroids were then treated with RSL3 or IKE in fresh medium for the indicated time and stained with Sytox Green to calculate cell death.

Generation of spheroids according to the organoid establishment protocol

Organoid establishment was performed with procedures similar to those described previously[43]. Briefly, HT29 colon cancer cells were digested by TrypLE (Gibco, catalogue no. 12605-028) and 2×10^3 cells plated into non-tissue culture-treated, 24-well plates, accompanied by the supplementation of Matrigel (Corning, catalogue no. 354234). After 7 d, organoids were generated and added into IKE (10 μM), RSL3 (10 μM) and Lipro-1 (1 μM) for 72 h treatment, and subsequently cells were embedded and captured by an inverted microscope (Nikon). Organoids were visualized by NIS Elements Viewer software 5.21.

Plasmid construction and transfection

For AHR, *ALDH1A3* and FSP1 overexpression, full-length AHR, *ALDH1A3* and FSP1 were inserted into pcDNA3.1 (Invitrogen) and Plenti4 vectors. For the sgRNAs of AHR, ALDH1A3, FSP1, DHODH and GCH1, these sgRNAs were constructed to PX458 and plenti-CRISPR-v.2 vectors. The sgRNA sequences were designed from the website (http://crispor.tefor.net). The primers are provided in Supplementary Table 5. Lipofectamine 3000 (Invitrogen) was used for plasmid transfection according to the manufacturer's protocols.

Quantitative PCR analysis

Total RNA was extracted using TRIzol (Invitrogen) according to the manufacturer's guidance and complementary DNA was synthesized using a reverse transcription kit (Thermo Fisher Scientific). The qPCR was performed using ultraSYBR Mixture (ComWin Biotech) on a CFX96 Real Time PCR Detection System (BioRad). These primers are provided in Supplementary Table 5.

ChIP assay

The assay was performed using ChIP kit (Cell Signaling Technology, catalogue no. 9003s) according to the manufacturer's protocol. In brief,

cells were cross-linked with 1% formaldehyde for 10 min at room temperature and neutralized with a final concentration of 0.125 M glycine. The harvested cells were suspended in cold lysis buffer. After a 10-min incubation at 4 °C, nuclei were harvested and lysed in ChIP buffer. After sonication, the lysates were centrifuged, the supernatants were added with magnetic beads coated with the specific AHR antibody (Cell Signaling Technology, catalogue no. 83200) and incubated overnight. Beads were washed three times with washing buffer and DNA was extracted using a spin column with the addition of DNA elution buffer and qPCR performed. *ALDH1A3* primers were provided in Supplementary Table 5.

Separation of cytoplasmic and nucleus fraction

Cells were suspended in buffer A (10 mM Hepes, pH 7.9, 10 mM KCl, 0.1 mM EDTA, 0.1 mM (ethylenebis(oxonitrilo))tetra-acetate (EGTA), 1 mM dithiothreitol (DTT), 0.15% NP-40 and protease inhibitor cocktail 1:100) and swollen for 10 min on ice. The cells were then centrifuged at 12,000*g* for 30 s. the supernatant was collected as a cytoplasmic extract and the pellet was washed with PBS. The pellet was resuspended in buffer B (10 mM Hepes, pH 7.9, 400 mM NaCl, 1 mM EDTA, 1 mM EGTA, 1 mM DTT, 0.15% NP-40 and protease inhibitor cocktail 1:100) and lysed for 15 min at 4 °C. The sample was centrifuged at 14,000*g* for 15 min at 4 °C. Equal amounts of proteins from cytosol and nucleus extract were subjected to western blotting.

NADH level measurement

For WT or *ALDH1A3* KO HT29 cells, 1×10^6 cells per sample, treated as indicated, were collected and intracellular NADH levels were determined using an NAD^+/NADH assay kit (Beyotime, catalogue no. S0175) according to the manufacturer's instructions.

CoQ and CoQH2 analysis

Collected cells were added with a total of 1,000 µl of extraction solution (ethanol–isopropanol, 95:5, precooled at −20 °C). After adding two small steel balls and 50 µl of butylated hydroxytoluene (concentration 5,000 µg ml^{-1}), the samples were vortexed for 30 s and then homogenized for 4 min and sonicated for 5 min in an ice-water bath. The homogenate and sonicate circle were repeated three times. The samples were incubated at −40 °C for 1 h and centrifugated at 12,000*g* and 4 °C for 15 min. A 950-µl aliquot of the supernatant was evaporated to dryness under a gentle stream of nitrogen and reconstituted in 100 µl of ethanol solution containing 5% formic acid. All the samples were vortexed for 30 s and sonicated for 5 min in the ice-water bath. After the samples were centrifuged at 12,000*g* for 15 min at 4 °C and the clear supernatant was subjected to ultrahigh-performance LC–tandem MS (UHPLC–MS/MS) analysis.

The UHPLC separation was carried out using an EXIONLC System (Sciex), equipped with a ZORBAX Eclipse Plus C18 Rapid Resolution HD, 2.1 × 50 mm^2, 1.8 µm. The mobile phase B was 60% isopropyl alcohol in methanol with 5 mM ammonium formate. The column temperature was set at 40 °C. The autosampler temperature was set at 4 °C and the injection volume was 2 µl. A SCIEX 6500 QTRAP+ triple quadrupole mass spectrometer (Sciex), equipped with an IonDrive Turbo V electrospray ionization (ESI) interface, was applied for assay development. Typical ion source parameters were: curtain gas = 35 p.s.i., ion spray voltage = 5,000 V, temperature = 450 °C, ion source gas 1 = 50 p.s.i. and ion source gas 2 = 50 p.s.i.

The multiple reaction monitoring (MRM) parameters for each of the targeted analytes were optimized using flow injection analysis, by injecting the standard solutions of the individual analytes into the ESI source of the mass spectrometer. Several most sensitive transitions were used in the MRM scan mode to optimize the collision energy. Among the optimized MRM transitions per analyte, the Q1/Q3 pairs that showed the highest sensitivity and selectivity were selected as 'quantifier' for quantitative monitoring. The additional transitions acted as 'qualifier' for the purpose of verifying the identity of the target analytes.

16S rRNA gene sequencing of faecal microbiota

To extract DNA from human faecal samples, 0.2 g of faecal pellets was collected in a standard 2-ml screw-cap, cryostorage vial. Then, 250 µl of 20% sodium dodecylsulfate, 500 µl of PCR-A (GeneJET PCR Purification Kit, Thermo Fisher Scientific, catalogue no. K0702), 250 µl of 0.1-mm zirconia/silica beads and 550 µl of phenol:chloroform:isoamyl alcohol were added to the cryostorage vials and bead beaten for 2 min in a high-speed Tissuelyser, followed by centrifugation at 9,000*g*. The aqueous phase, 500 µl, was removed and run through a PCR purification column (GeneJET PCR Purification Kit). The V4 region of the 16S rRNA gene amplicons was generated using the primer pair 515F/806R (515F: 5′-GTGYCAGCMGCCGCGGTAA-3′, 806R: 5′-GGACTACNVGGGTWTCTAAT-3′). PCR products were quantified, pooled and cleaned using the PCR Cleanup kit (QIAGEN) and subsequently sequenced on Illumina MiSeq (2 × 250 bp). Demultiplexed fastq-files of forward and reverse reads were analysed using QIIME2 (Quantitative Insights Into Microbial Ecology2). Features with read number <0.001% of the total read frequency were removed from the analysis. Sequences were corrected and quality filtered using the DADA2 package integrated in QIIME2. A total of 942,793 sequences of 67 samples was achieved to a depth of 14,285 ± 4,096 reads (mean ± s.d.), with a maximum of 28,844 sequences and a minimum of 4,530 sequences per sample. Assigning taxonomy to sequences was performed with a Naïve Bayes classifier, trained on the Greengenes 13_8 99% operational taxonomic units with the q2-feature-classifier plugin.

The Mann–Whitney *U*-test using Prism (GraphPad, v.8.0.1) was performed to identify the difference in abundance of *Peptostreptococcus* occurrence between faecal communities of healthy people and patients with CRC.

LC–MS-based metabolomics analysis of tryptophan metabolites in vitro

Accurate mass LC–MS was performed on an AB TripleTOF operating in IDA mode as previously described[28]. In brief, *P. anaerobius* were grown in 15 ml of GAM medium. Then, 48 h after liquid culture, bacterial supernatant was collected by centrifugation at 3,000*g* for 10 min. Bacterial supernatant was mixed with acetonitrile in a 1:1 ratio. Magnesium sulfate (0.2 g ml^{-1}) and sodium acetate (0.05 g ml^{-1}) were added and shaken for 10 min followed by centrifugation at 3,000 r.p.m. The organic phase was dried in a Termovap Sample Concentrator.

The total organic extract of *P. anaerobius* culture was solubilized in starting mobile phase (95:5, A:B) and 1 µl of material was separated over a Waters Acquity BEH C18 column (2.1 × 100 mm^2, 2.5 µm) coupled to a Waters Acquity BEH C18 VanGuard precolumn (2.1 × 5 mm^2, 2.5 µm). Data analysis was performed using PeakView 1.2 software.

LC–MS-based analysis of tryptophan metabolites in vivo

To quantify the level of tryptophan metabolites in *P. anaerobius*-colonized mice, 150 µl of serum from germ-free and monocolonized mice was mixed with 1 ml of methanol and acetonitrile (1:1, v/v) and then ultrasonicated in a water bath for 10 min. After centrifugation at 12,000*g* for 10 min, 800 µl of supernatant was transferred into an LC-sampling vial for LC–MS analysis.

To measure the concentration of IDA in human faeces, 100 mg of faeces was mixed with 200 µl of water. Next, the samples were mixed with 1 ml of methanol and acetonitrile (1:1, v/v) and vortexed for 10 s, followed by ultrasonication in a water bath for 10 min. Samples were frozen in liquid nitrogen, thawed at room temperature and then sonicated for 10 min. The operations above were repeated three times in total. After incubation at −20 °C for 2 h, 800 µl of supernatant of each sample was filtered through a 0.22-µm microfilter and transferred into an LC-sampling vial for LC–MS analysis.

A UHPLC LC-30 system, coupled with an LC–MS/MS 8050 mass spectrometer, was used to analyse the tryptophan metabolites in ESI-positive ion mode. In brief, 1 µl of sample was added into the Waters

ACQUITY UPLC C18 column (1.7 μm, 2.1 × 100 mm^2). The flow rate was 0.3 ml min^{-1} and the column temperature was 35 °C. Mobile phase A consisted of 0.1% formic acid in water and mobile phase B of 0.1% formic acid in acetonitrile. All samples were eluted with a binary gradient: 0 min, 5% B; 2 min, 5% B; 20 min, 40% B; 22 min, 98% B; 24 min, 98% B; and 24.5 min, 5% B.

LC–MS analysis of phospholipids

For exploring the effect of IDA in phospholipid synthesis, HT29 cells with IDA treatment were collected and analysed for phospholipid composition according to a previous description[42].

Pharmacokinetics for IDA contents in vivo

To explore the metabolic characteristics and physiological concentration of IDA in vivo, 8-week-old C57BL/6J mice were injected i.p. with IDA (50 mg kg^{-1}). Plasma was collected at 0, 1, 2, 4, 8, 12, 24 and 48 h and the contents of IDA in plasma were measured using LC–MS. The different concentration of standard IDA samples was used as a positive control for depicting the standard curve.

FlAsH sensor-based BRET assay

To characterize the binding properties of IDA to AHR, a FlAsH sensor-based BRET assay was performed as previously described[44]. Briefly, HEK293 cells transfected with AHR FlAsH BRET sensors (site 1, s1: FTPIGCD^{301}-CCPGCC-A^{302}KGRIVL; and site 2, s2: KGRIVLG^{309}-CCPGCC-Y^{310}TEAELC) were seeded into a six-well plate and incubated for 48 h at 37 °C in 5% CO_2. HEK293 cells overexpressing AHR FlAsH BRET sensors were washed with a Fluorescent arsenical hairpin (FlAsH) BRET buffer containing 25 mM Hepes, 140 mM NaCl, 0.9 mM $MgCl_2$, 2.7 mM KCl, 1 mM $CaCl_2$, 0.37 mM NaH_2PO_4, 12 mM $NaHCO_3$ and 5.5 mM D-glucose and further incubated with FlAsH-EDT2 (prediluted at a final concentration of 2.5 μM) for 30 min at 37 °C in 5% CO_2. Afterwards, the cells were washed twice, resuspended in FlAsH BRET buffer and subsequently seeded into 96-well plates (black wall, clear bottom) at a density of 1 × 10^5 per well. The cells were treated with an increasing concentration of IDA together with 5 μM coelenterazine-h; the BRET signals between Nluc (440–480 nm) and FlAsH fluorescent moiety (525–585 nm) emissions were determined using a Mithras LB 940 Multimode Microplate Reader.

Measurement of *ALDH1A3* enzymatic activity

Cells overexpressing flag-*ALDH1A3* or *ALDH1A3* KO cells were lysed in 0.5 ml of buffer containing 50 mM Tris, pH 8.0, 25 mM EDTA, 5 mM 2-mercaptoethanol and 1 mM phenylmethylsulfonyl fluoride for 30 min. Cells were then centrifuged at 12,000*g* for 10 min at 4 °C and the supernatants were collected. For in vitro enzymatic assay, purified ALDH1A3 proteins were enriched using flag beads. For in vivo enzymatic assay, the protein concentration was determined using a BCA kit. Aliquots of 200 μl incubated at 37 °C with the addition of purified ALDH1A3 or protein extract, 5 mM NAD^+ and 1 mM all-*trans*-retinol as substrate were used to measure the change in absorbance at 340 nm at the indicated time point. A control reaction in which all-*trans*-retinol was not added monitored the endogenous rate of NAD^+ reduction.

Xenograft experiment

In a HT29 tumour-bearing xenograft, 1 × 10^6 HT29 cells were injected subcutaneously into the dorsal region in 6- or 7-week-old, male nude mice (Charles River Laboratories) and then IDA (50 mg kg^{-1}) and Lipro-1 (10 mg kg^{-1}) were administered in situ three times a week.

In an MC38 tumour-bearing xenograft, 3 × 10^5 MC38 cells were administered subcutaneously in immunocompetent 6 week-old male C57BL/6J mice purchased from Charles River Laboratories. The next day, IDA (50 mg kg^{-1}; Sigma-Aldrich, catalogue no. I3807) or Lipro-1 (10 mg kg^{-1}) was individually administered i.p. to C57BL/6J mice three times a week.

To observe the role of *ALDH1A3* in IDA-mediated tumour ferroptosis in vivo, the *ALDH1* enzymatic inhibitor disulfiram (50 mg kg^{-1}, TargetMol, catalogue no. T0054) and α-tocopherol (10 mg kg^{-1}; Selleck, catalogue no. S6104) were administered i.p. for 14 d consecutively.

To investigate whether AHR or *ALDH1A3* is involved in IDA-mediated tumorigenesis promotion, HT29 AHR and *ALDH1A3* KO cell lines were constructed, and 1 × 10^6 HT29 KO cells and its control cells were individually injected subcutaneously on both sides of the dorsal side of nude mice. The next day, IDA (50 mg kg^{-1}, Sigma-Aldrich, catalogue no. I3807) was administered i.p. for 12 d consecutively. Tumour size was measured every 2–3 d for 4–5 weeks and tumour volume was calculated: volume (cm^3) = (length × width^2) × 0.5. The maximal tumour size/burden permitted by the ethics committee or institutional review board is 2,000 mm^3, and all our maximal tumour sizes/burdens were not exceeded. The number of mice in these experiments is described in the corresponding figure legends (Figs. 2e–j, 3k–n, 4i–j and 5k,l and Extended Data Figs. 8d–l and 10p).

Apc$^{Min/+}$ tumour model

The 8-week-old male C57BL/6 *Apc*$^{Min/+}$ mice (GemPharmatech Co., Ltd) were pretreated with antibiotics (ampicillin (1 g l^{-1}), vancomycin (0.5 g l^{-1}), metronidazole (1 g l^{-1}) and neomycin (1 g l^{-1})) for 2 weeks via drinking water. For implantation of *P. anaerobius*, mice were gavaged with PBS or 10^8 colony-forming units (c.f.u.) of *P. anaerobius* daily until the end of the experiment, and then the mice were killed at 20 weeks. For supplementation of IDA, the mice were treated with IDA (50 mg kg^{-1}) injected i.p. for 15 weeks. Then, the small and large intestines were dissected and flushed with PBS. The whole intestines were opened flat for tumour counting or Swiss-rolled and fixed in 10% formalin for haematoxylin and eosin (H&E) staining. The number of mice in these experiments is described in the corresponding figure legends (Figs. 7e–j,n–o).

AOM/DSS model of colitis-associated cancer

Male C57BL/6J mice aged 8 weeks (Charles River Laboratories) were used to establish the colitis-associated cancer model pretreated with microbiota depletion using antibiotics for 1 week, and then induced by AOM injection (i.p. 12 mg kg^{-1}) at day 0 and fed with 3% DSS solubilized in water at days 3, 25 and 45 for 5 d. To explore the function of IDA and *P. anaerobius* in tumorigenesis, IDA (50 mg kg^{-1}, daily) injected i.p. and *P. anaerobius* gavaging (10^8 c.f.u., daily) were practised for 3 weeks. Eventually, mice were euthanized and the tumours in large intestines were counted and embedded in paraffin for further analysis. The number of mice in these experiments is described in the corresponding figure legends (Fig. 7p–q and Extended Data Fig. 10o).

P. anaerobius implantation in germ-free mice and intratumoral injection in C57BL/6J mice

To explore the characteristics of *P. anaerobius* in vivo, 12-week-old, male, germ-free C57BL/6J mice were purchased from Cyagen Biosciences and bred in germ-free flexible film isolators (Class Biologically Clean) throughout the present study. Germ-free C57BL/6 mice were orally inoculated by gavage with *P. anaerobius* (0.8 optical density (OD), 200 μl) and serum was collected for LC–MS analysis after 3 d. The number of mice in these experiments is described in the corresponding figure legend (Fig. 7k–m).

To explore the physiological function of *P. anaerobius* and IDA in vivo, MC38 tumour-bearing, 6-week-old, female C57BL/6J mice (Charles River Laboratories) supplemented with PBS, *E. coli* or *P. anaerobius* (1 × 10^8 c.f.u.) were injected intratumorally once every 2 d. The tumour tissues were collected in the indicated time for further study. The number of mice in these experiments is described in the corresponding figure legends (Fig. 7a–d and Extended Data Fig. 10m).

Patient specimens and IHC

The faecal samples for *P. anaerobius* enrichments and IDA contents were collected from 35- to 75-year-old male and female patients with CRC derived from the First Affiliated Hospital of USTC, and corresponding age- and sex-matched healthy controls selected from the Physical Examination Center of the First Affiliated Hospital of USTC. The study was approved by the Ethics Committee of USTC. The number of participants in these experiments is described in the corresponding figure legend (Fig. 6a–d).

Human colon cancer samples were collected from Shandong Provincial Hospital (Jinan, China). The study was approved by the Ethics Committee of Shandong University and informed consent was obtained from the patients involved.

IHC was performed with procedures similar to those described previously. Briefly, the fresh tissues were fixed in paraformaldehyde and embedded in paraffin for sectioning. Sections were incubated individually with primary antibodies against 4-HNE (1:200, Abcam, catalogue no. ab46545), MDA (1:200; Adipogen, catalogue no. JAI-MMD-030N), 8-OHDG (1:200; Abcam, catalogue no. ab48508), AHR (1:1,000; Cell Signaling Technology, catalogue no. 83200) and *ALDH1A3* (1:200, Proteintech, catalogue no. 25167-1-AP) in a humidified chamber at 4 °C overnight. The IHC images were photographed on an ortho microscope (Olympus) and mean OD values for each specimen were calculated using Image-pro plus software[20,42].

Statistics and reproducibility

Information on the number of biologically independent samples analysed and the number of times experiments were performed is included in the figure legends. All the representative experiments were repeated three times independently with similar results. All statistical tests performed were two sided except when noted. No statistical methods were used to predetermine sample sizes, but our sample sizes are similar to those reported in previous publications[45–47]. Data distribution was assumed to be normal but this was not formally tested. No data were excluded from the analyses and biological samples were excluded from the study only if sample preparation or data acquisition failed. For both in vitro and in vivo experiments, samples/animals were assigned to experimental groups using simple randomization and the investigators were not blinded to allocation during experiments and outcome assessment.

Reporting summary

Further information on research design is available in the Nature Portfolio Reporting Summary linked to this article.

Data availability

The survival curve data of AHR gene expression data in human cancer tissues were derived from The Cancer Genome Atlas (TCGA) database and in human cancer cell lines from the Cancer Cell Line Encyclopedia (CCLE; https://portals.broadinstitute.org/ccle). The correlation of AHR and *ALDH1A3* in human cancer tissues was derived from Gene Expression Profiling Interactive Analysis (http://gepia2.cancer-pku.cn). The expression of AHR and *ALDH1A3* was derived from Oncomine (https://www.oncomine.org). ChIP–seq data of AHR are available from the database (http://chip-atlas.org). RNA-seq data are provided as Supplementary tables. Source data are provided with this paper.

Code availability

All packages used for data analysis are publicly available. No customized code was generated for the present study. All scripts used for bulk RNA-seq data analyses in the present study are provided as Supplementary tables.

References

42. Liu, D. et al. Tryptophan metabolism acts as a new anti-ferroptotic pathway to mediate tumor growth. *Adv. Sci.* **10**, e2204006 (2023).
43. Cattaneo, C. M. et al. Tumor organoid-T-cell coculture systems. *Nat. Protoc.* **15**, 15–39 (2020).
44. Ping, Y. Q. et al. Structures of the glucocorticoid-bound adhesion receptor GPR97-Go complex. *Nature* **589**, 620–626 (2021).
45. Collignon, E. et al. m6A RNA methylation orchestrates transcriptional dormancy during paused pluripotency. *Nat. Cell Biol.* **25**, 1279–1289 (2023).
46. Duplaquet, L. et al. KDM6A epigenetically regulates subtype plasticity in small cell lung cancer. *Nat. Cell Biol.* **25**, 1346–1358 (2023).
47. Hoetker, M. S. et al. H3K36 methylation maintains cell identity by regulating opposing lineage programmes. *Nat. Cell Biol.* **25**, 1121–1134 (2023).

Acknowledgements

This work was supported by the National Key R&D Program of China (grant nos. 2022YFA0912600 to B.C. and 2021YFA1101300 and 2020YFA0112503 to R.C.), National Natural Science Foundation of China (grant nos. 32000515 to B.C., 82325025 to S.Z. and 82030029 and 81970882 to R.C.), Natural Science Foundation of Shandong Province (grant no. ZR2020QC074 to B.C.), Taishan Scholars Program (grant no. TSQN201909030 to B.C.) of Shandong Province, Cutting Edge Development Fund of Advanced Medical Research Institute (to B.C.), Strategic Priority Research Program of the Chinese Academy of Science (grant no. XDA16010303 to R.C.), Natural Science Foundation from Jiangsu Province (grant no. BE2019711 to R.C.) and Science and Technology Department of Sichuan Province (grant no. 2021YFS0371 to R.C.). Model diagrams of the animal experiment in Fig. 7 were created with BioRender.com.

Author contributions

W.C., M.G. and D.L. performed most experiments with assistance from P.X., C.Y., C.L., Y.Y., Yudan Z., J.L. and X.F. Yongchun Z. and H.H. performed organoid experiments. L.D., S.S. and Y.X. collected clinical samples. J.C. and Z.H. analysed intestinal microbial data. B.C. and S.Z. designed the experiments. B.C. supervised the study, established collaborations, allocated funding for the present study and wrote most of the manuscript with the assistance of J.S., R.C., W.G. and S.Z. B.C. had the role of conceptualization, design and preparation of the manuscript and R.C. and S.Z. in preparation of the manuscript. All the authors commented on the manuscript.

Competing interests

The authors declare no competing interests.

Additional information

Extended data is available for this paper at https://doi.org/10.1038/s41556-023-01314-6.

Supplementary information The online version contains supplementary material available at https://doi.org/10.1038/s41556-023-01314-6.

Correspondence and requests for materials should be addressed to Wei Gu, Renjie Chai, Shu Zhu or Bo Chu.

Peer review information *Nature Cell Biology* thanks Ömer Yilmaz and the other, anonymous, reviewer(s) for their contribution to the peer review of this work. Peer reviewer reports are available.

https://doi.org/10.1038/s41556-023-01314-6

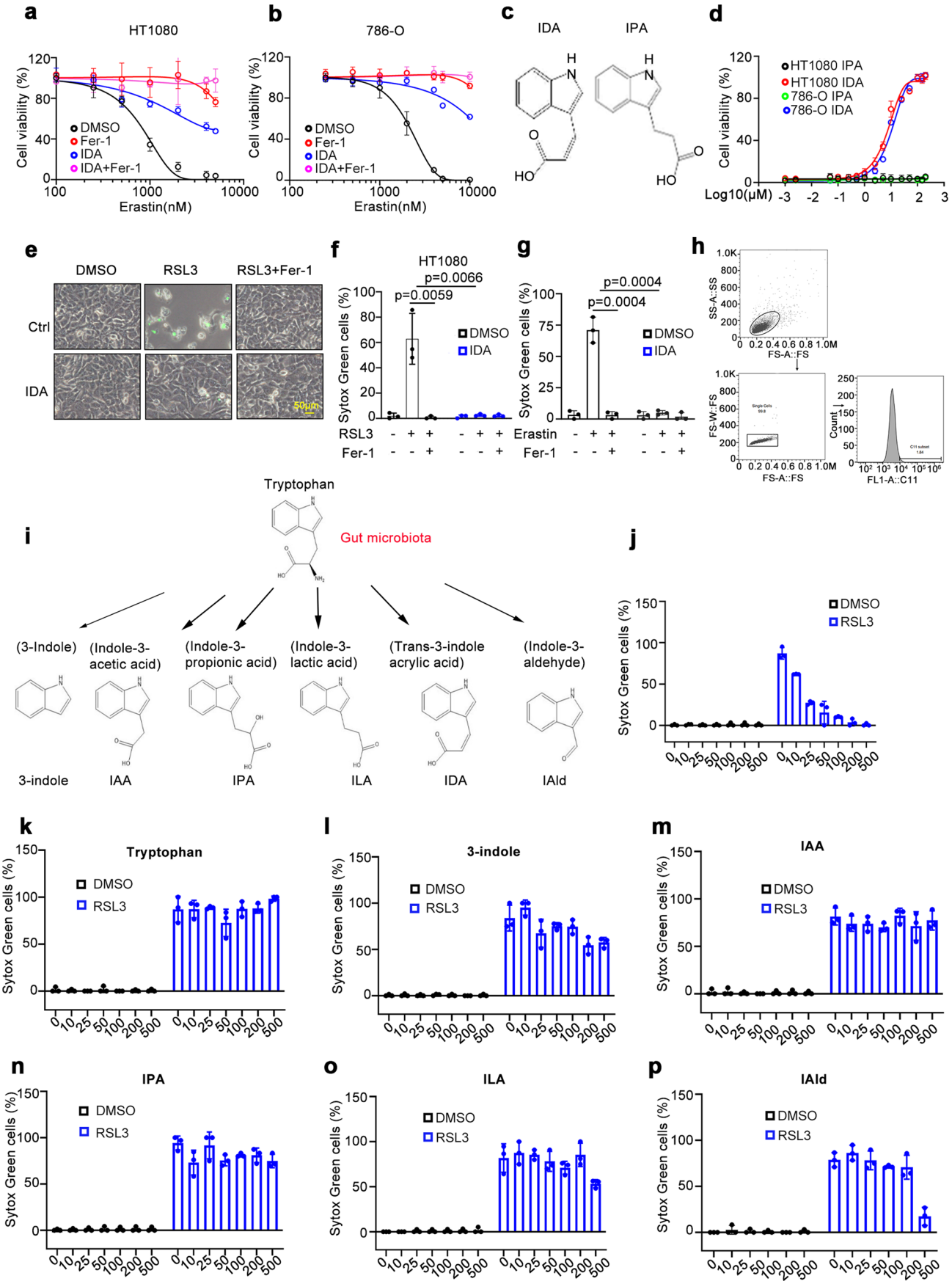

Extended Data Fig. 1 | See next page for caption.

https://doi.org/10.1038/s41556-023-01314-6

Extended Data Fig. 1 | IDA but not any other tryptophan metabolites renders cells resistant to ferroptosis. (a, b) Dose-dependent toxicity of erastin induced cell death of HT1080 (a) and 786-O cells (b) supplemented with IDA (50 μM). Cell viability was assessed 24 h thereafter using CCK8. (c) Chemical structure of IDA and IPA. (d) Cell viability of HT1080 and 786-O cells treated with RSL3 (1 μM) and indicated concentration of IDA or IPA for 24 h. (e, f) Representative phase-contrast images of HT1080 cells (e) incubated with IDA (50 μM) for 12 h were treated with RSL3 (200 nM) and Fer-1 (1 μM). Dead cells stained with Sytox Green were calculated (f). Scale bars, 50 μm. (g) Cell death of HT1080 cells treated with erastin (5 μM), IDA (50 μM) and Fer-1 (1 μM) for 24 h. (h) FACS sequential gating strategies for C11-BODIPY 581/591 staining of lipid peroxidation were shown. (i) Chemical structure of tryptophan derivates derived from gut microbiota. (j-p) Cell death in HT1080 cells treated with RSL3 (200 nM) and indicated concentration of tryptophan derivates ranging from 10 μM to 500 μM for 16 h. Data and error bars are mean ± s.d., n = 3 biological independent experiments in a, b, d, f, g and j-p. All P values were calculated using two-tailed unpaired Student's t-test.

https://doi.org/10.1038/s41556-023-01314-6

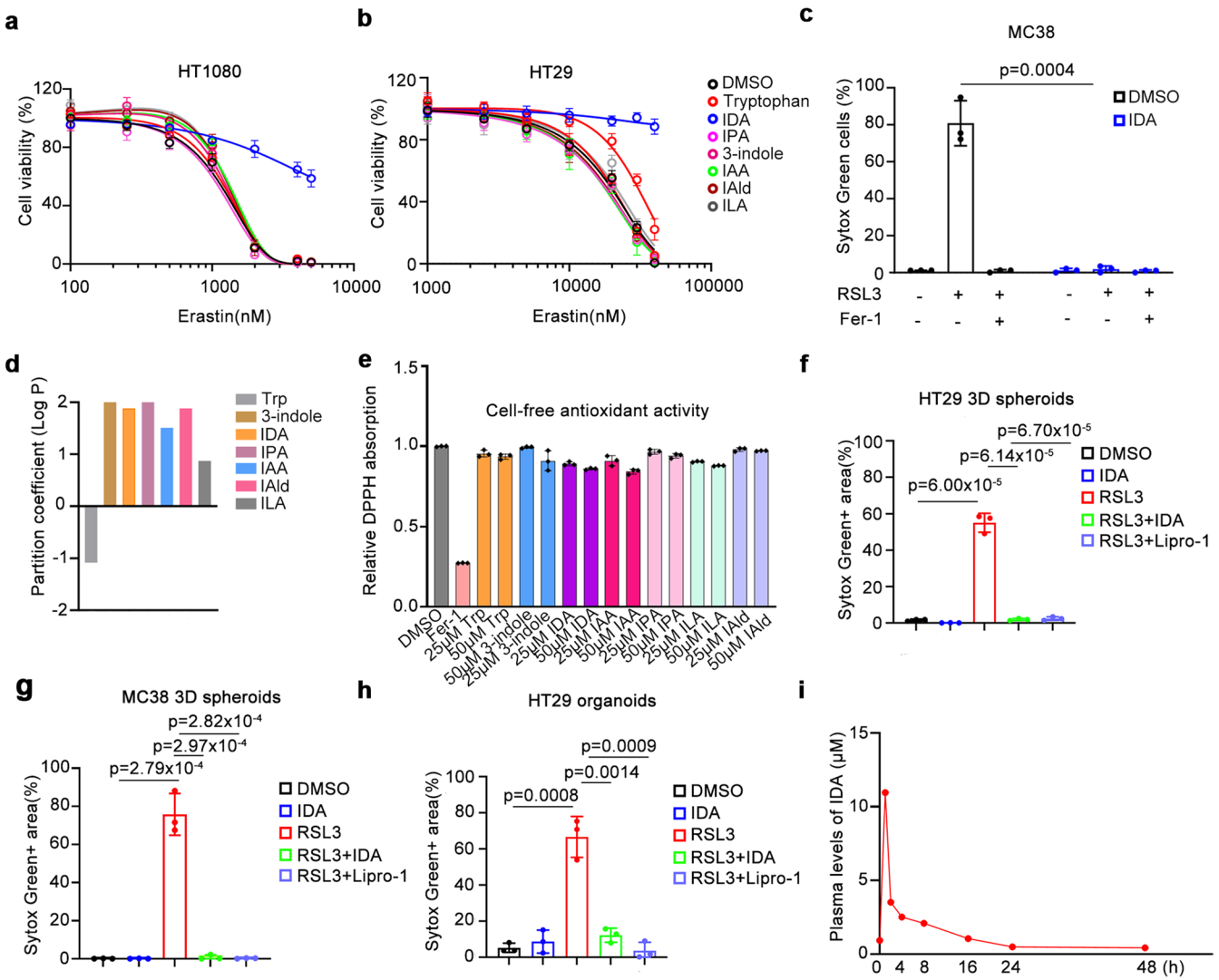

Extended Data Fig. 2 | IDA-mediated ferroptosis inhibition is independent of RTA activity and promotes tumour growth both *in vitro* and *in vivo*. (a, b) Cell viability in HT1080 (a) and HT29 cells (b) treated with erastin and the indicated tryptophan metabolites for 24 h. Tryptophan (50 μM), IDA (50 μM), IPA (50 μM), 3-indole (50 μM), Indole-3-acetic acid (IAA, 50 μM), indole-3-aldehyde (IAld, 50 μM) and Indole-3-lactic acid (ILA, 50 μM). (c) Cell death of MC38 cells treated with RSL3 (5 μM), IDA (50 μM) and Fer-1 (1 μM) for 12 h. (d) Predicted lipophilicity of the tryptophan metabolites (https://molinspiration.com/cgi-bin/properties). (e) DPPH assay to test the ability of the tryptophan metabolites as radical trapping agent. (f) HT29 3D Spheroids treated with RSL3 (5 μM), IDA (100 μM) and Lipro-1(1 μM) for 48 h and then sytox green positive area was calculated. (g) MC38 3D Spheroids treated with RSL3 (5 μM), IDA (100 μM) and Lipro-1(1 μM) for 48 h and then sytox green positive area was calculated. (h) HT29 organoids treated with RSL3 (5 μM), IDA (200 μM) and Lipro-1(1 μM) for 72 h and then sytox green positive area was calculated. (i) LC-MS analysis of IDA content in plasma of *C57BL/6 J* mice via intraperitoneal administration of 50 mg/kg IDA. Data and error bars are mean ± s.d., n = 3 biological independent experiments in a-c, e-h. All P values were calculated using two-tailed unpaired Student's t-test.

https://doi.org/10.1038/s41556-023-01314-6

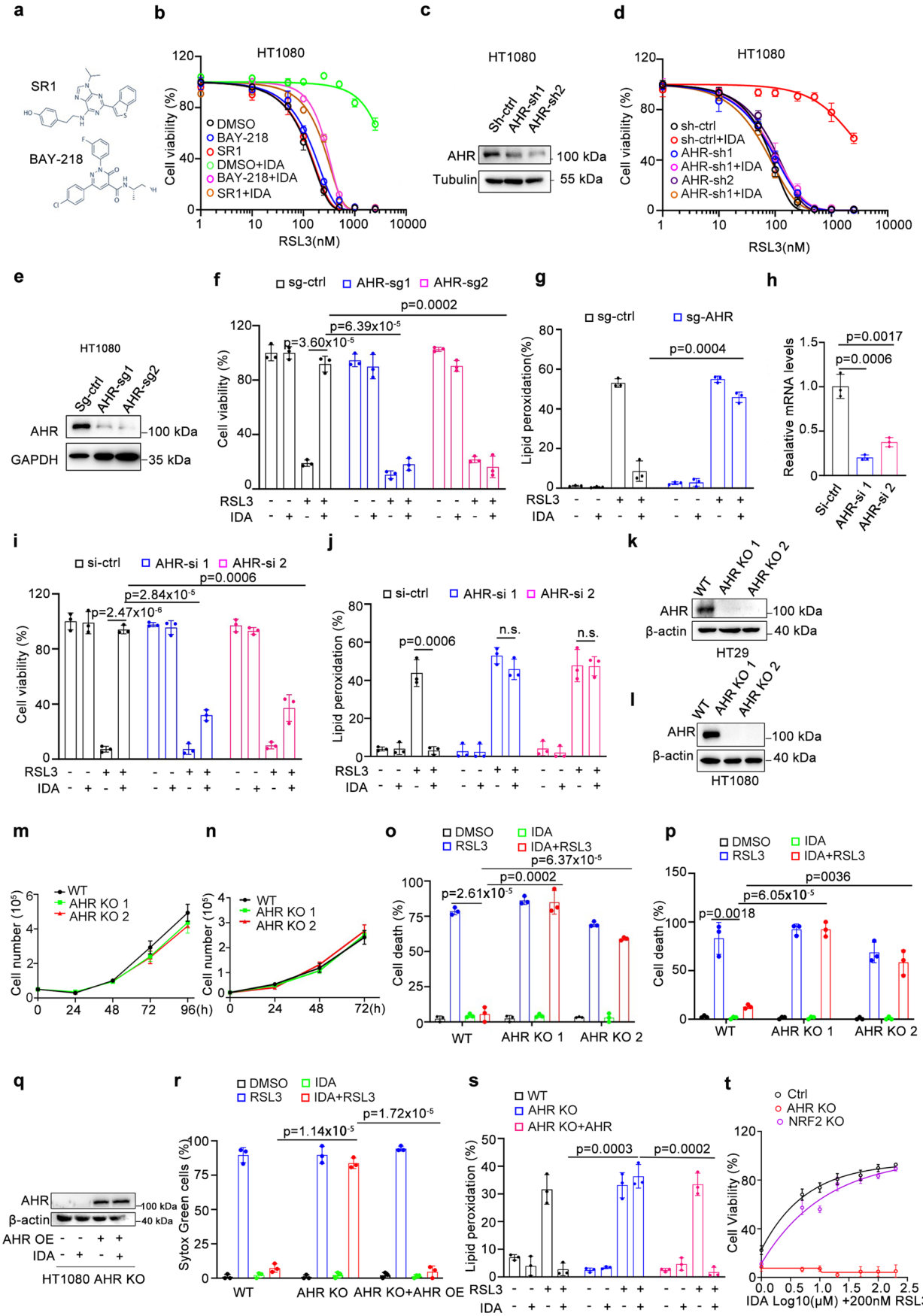

Extended Data Fig. 3 | See next page for caption.

https://doi.org/10.1038/s41556-023-01314-6

Extended Data Fig. 3 | IDA-mediated ferroptosis resistance is dependent of AHR. (a) Chemical structure of AHR antagonists BAY-218 and SR1. (b) Cell viability of HT1080 cells treated with RSL3, IDA (50 μM), BAY-218 (10 μM) and SR1 (10 μM) for 24 h. (c) Western blot analysis of HT1080 cells expressing shRNA-ctrl or AHR-shRNA. (d) Cell viability in HT1080 cells expressing shRNA-ctrl or AHR-shRNA treated with RSL3 (200 nM) and IDA (50 μM) for 24 h. (e) Western blot analysis of HT1080 cells expressing sg-ctrl or sg-AHR. (f, g) Cell viability (f) and lipid peroxidation (g) of HT1080 cells expressing sg-ctrl or AHR-sg treated with RSL3 (200 nM) and IDA (50 μM). (h) Relative mRNA levels of AHR in MC38 cells transfected with AHR siRNA. (I, j) Cell viability (i) and lipid peroxidation (j) of MC38 cells with AHR siRNA treated with RSL3 (5 μM) and IDA (50 μM). (k) Western blot analysis of AHR in HT29 WT and AHR KO cells. (l) Western blot analysis of AHR in HT1080 WT and AHR KO cells. (m) Cell growth curve of HT29 WT and AHR KO cells for the indicated time. (n) Cell growth curve of HT1080 WT and AHR KO cells for the indicated time. (o, p) Cell death of HT29 AHR KO (o) and HT1080 AHR KO cells (p) treated with RSL3 and IDA (50 μM) for 8 h. (q) Western blot analysis of AHR in HT1080 AHR KO cells with ectopic expression of AHR. (r) HT1080 AHR KO cells with ectopic expression of AHR treated with RSL3 (200 nM) and IDA (50 μM) and then sytox green positive area was calculated. (s) Lipid peroxidation of HT1080 AHR KO cells with ectopic expression of AHR treated with RSL3 (200 nM) and IDA (50 μM). (t) Cell viability of WT, AHR KO, NRF2 KO HT1080 cells upon RSL3 and a titration of IDA treatment. The concentration of IDA is 5, 10, 20, 50, 100, 200 μM. The Western blot experiments were repeated three times independently with similar results in c, e, k, l and q. Data and error bars are mean ± s.d., n = 3 biological independent experiments in b, d, f-j, m-p and r-t. All P values were calculated using two-tailed unpaired Student's t-test.

https://doi.org/10.1038/s41556-023-01314-6

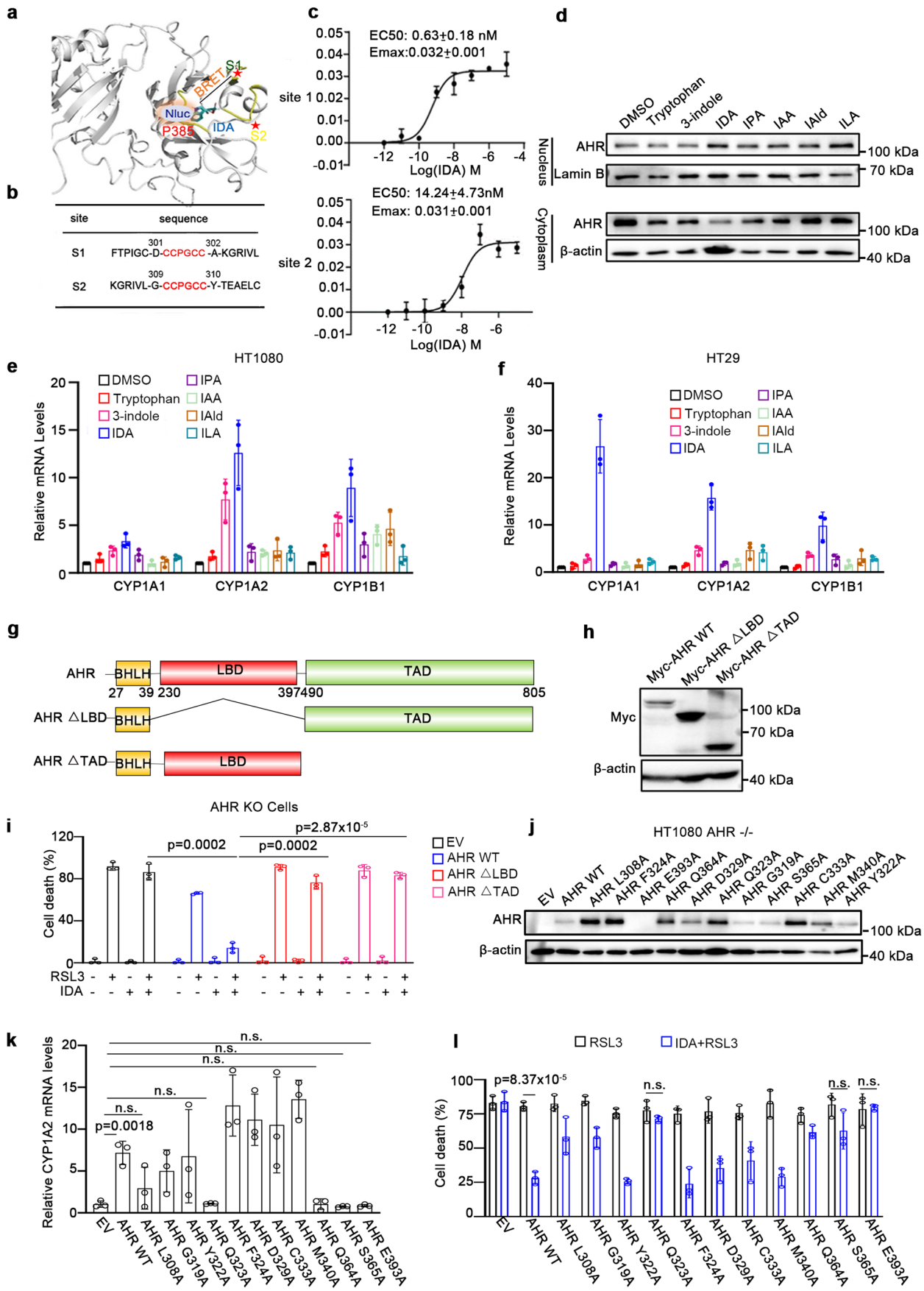

Extended Data Fig. 4 | See next page for caption.

https://doi.org/10.1038/s41556-023-01314-6

Extended Data Fig. 4 | The ligand-binding domain of AHR is critical for IDA-mediated ferroptosis. (a) Schematic representation of the FlAsH-BRET assay design. The Nluc was inserted at the N terminus of wild-type AHR, and the FlAsH motif were inserted in the designated positions in the figure. FlAsH motifs are labelled in red. The specific residues that interact with the ligand are highlighted in yellow. (b, c) Representative dose response curve of the BCM-induced BRET ratio in HEK293 cells overexpressing two FlAsH-BRET sensors 309 (b) and 301(c) sites using FlAsH-BRET assay. (d) Western blotting showing AHR protein levels in nucleus and cytoplasm fractions from HT29 cells upon IDA (50 μM) treatment for 2 h. (e, f) mRNA levels of AHR target genes in HT1080 (e) and HT29 cells (f) upon supplementation of tryptophan metabolites. Tryptophan (50 μM), IDA (50 μM), IPA (50 μM), 3-indole (50 μM), Indole-3-acetic acid (IAA, 50 μM), indole-3-aldehyde (IAld, 50 μM) and Indole-3-lactic acid (ILA, 50 μM). (g) Schematic diagram of WT, ligand binding domain-deficient (ΔLBD) and transactivation domain-deficient (ΔTAD) AHR. (h) Western blot analysis of expression of WT, ΔLBD and ΔTAD AHR in HT1080 AHR KO cells. (i) Cell death in HT1080 AHR KO cells expressing WT, ΔLBD and ΔTAD AHR treated with RSL3 (200 nM) and IDA (50 μM) for 8 h. (j) Western blot analysis of HT1080 AHR KO cells transfected with indicated mutant AHR constructs. (k) mRNA levels of CYP1A2 in HT1080 AHR KO cells transfected with indicated mutant AHR constructs upon IDA treatment. (l) Cell death of HT1080 AHR KO cells transfected with indicated mutant AHR constructs. The Western blot experiments were repeated three times independently with similar results in d, h and j. Data and error bars are mean ± s.d., n = 3 biological independent experiments in c, e, f, i, k, l. All P values were calculated using two-tailed unpaired Student's t-test.

https://doi.org/10.1038/s41556-023-01314-6

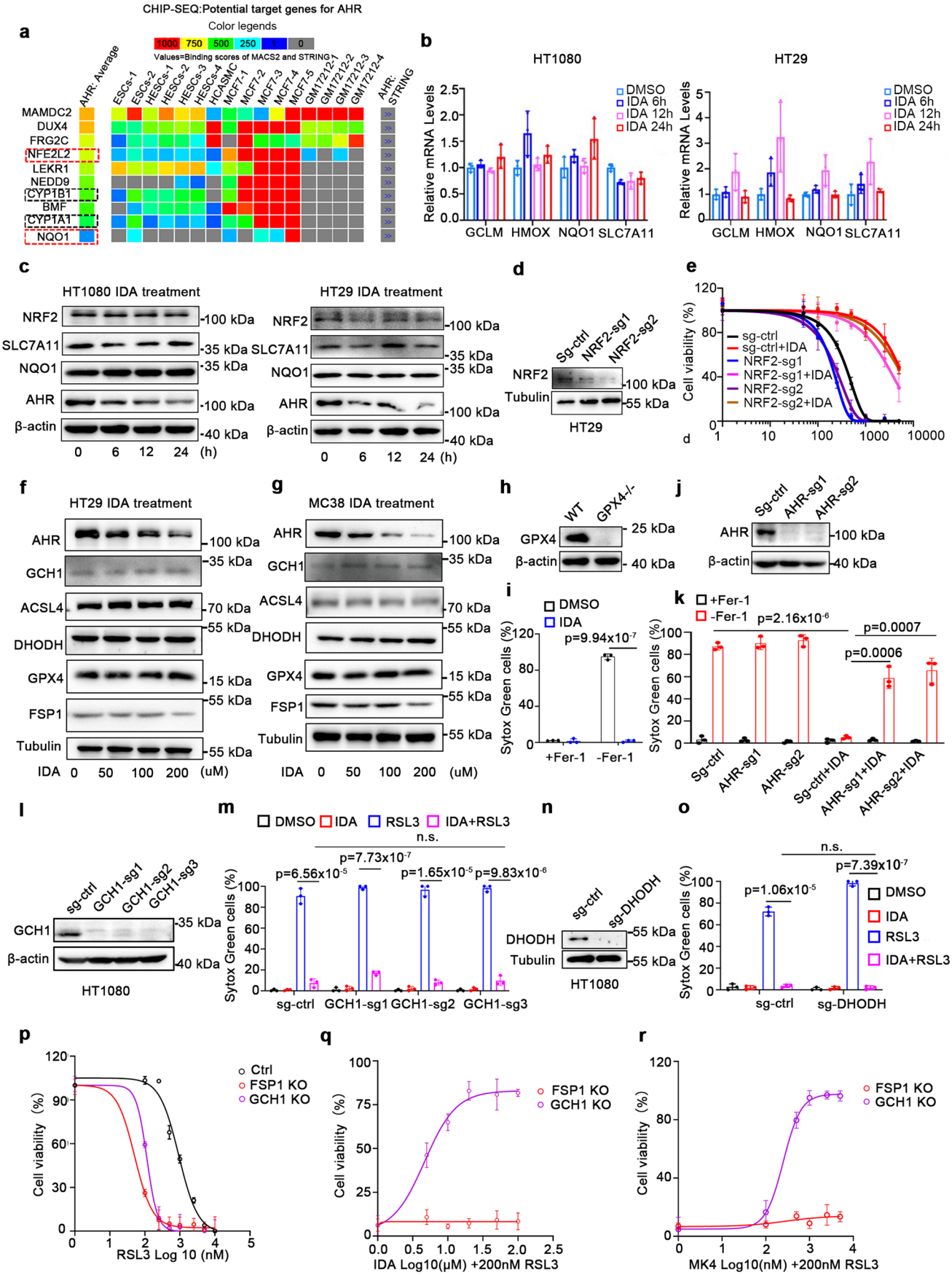

Extended Data Fig. 5 | See next page for caption.

https://doi.org/10.1038/s41556-023-01314-6

Extended Data Fig. 5 | IDA-mediated ferroptosis inhibition is independent of NRF2 and classical ferroptosis-ralated genes. (a) ChIP-SEQ analysis of potentially regulated genes by AHR from ChIP-Altas database (http://chip-atlas.org/). (b) mRNA levels of NRF2 target genes involved in ferroptosis in HT1080 and HT29 upon IDA (50 μM) treatment. (c) Western blotting showing levels of NRF2 target genes in HT1080 and HT29 upon IDA (50 μM) treatment for the indicated time. (d) Western blot analysis of NRF2 expression in HT1080 cells expressing NRF2-sgRNA. (e) Cell viability in HT1080 cells expressing sg-ctrl or NRF2-sg treated with RSL3 and IDA (50 μM) for 24 h. (f, g) Western blot analysis of classical ferroptosis-related genes expression in HT29 (f) and MC38 (g) upon indicated concentration of IDA treatment. (h) Western blot analysis of GPX4 expression in HT1080 GPX4 KO cells. (i) Cell death of HT1080 GPX4 KO cells incubated with IDA (50 μM) with or without Fer-1 (1 μM) treatment. (j) Western blot analysis of AHR expression in HT1080 GPX4 KO cells expressing AHR-sgRNA. (k) Cell death in HT1080 GPX4 KO cells expressing AHR-sgRNA upon treatment with IDA (50 μM) or Fer-1 (1 μM). (l) Western blot analysis of GCH1 expression in HT1080 WT and GCH1 KO cells. (m) Analysis of cell death in HT1080 WT and GCH1 KO cells treated with IDA (50 μM) or RSL3 (200 nM). (n) Western blot analysis of DHODH expression in HT1080 DHODH KO cells. (o) Analysis of cell death in HT1080 WT and DHODH KO cells treated with IDA (50 μM) or RSL3 (200 nM). (p) Cell viability of HT1080 WT, FSP1 KO, GCH1 KO cells for the indicated concentrations of RSL3. (q, r) Cell viability of FSP1 KO and GCH1 KO cells upon RSL3 (200 nM) and a titration of IDA (q) or MK4 (r) treatment. The concentration of IDA is 5, 10, 20, 50, 100 μM. The concentration of MK4 is 100, 500, 1000, 2500, 5000 nM. The Western blot experiments were repeated three times independently with similar results in c, f-h, j, l and n. Data and error bars are mean ± s.d., n = 3 biological independent experiments in b, c, e, i, k, m and o-r. All P values were calculated using two-tailed unpaired Student's t-test.

https://doi.org/10.1038/s41556-023-01314-6

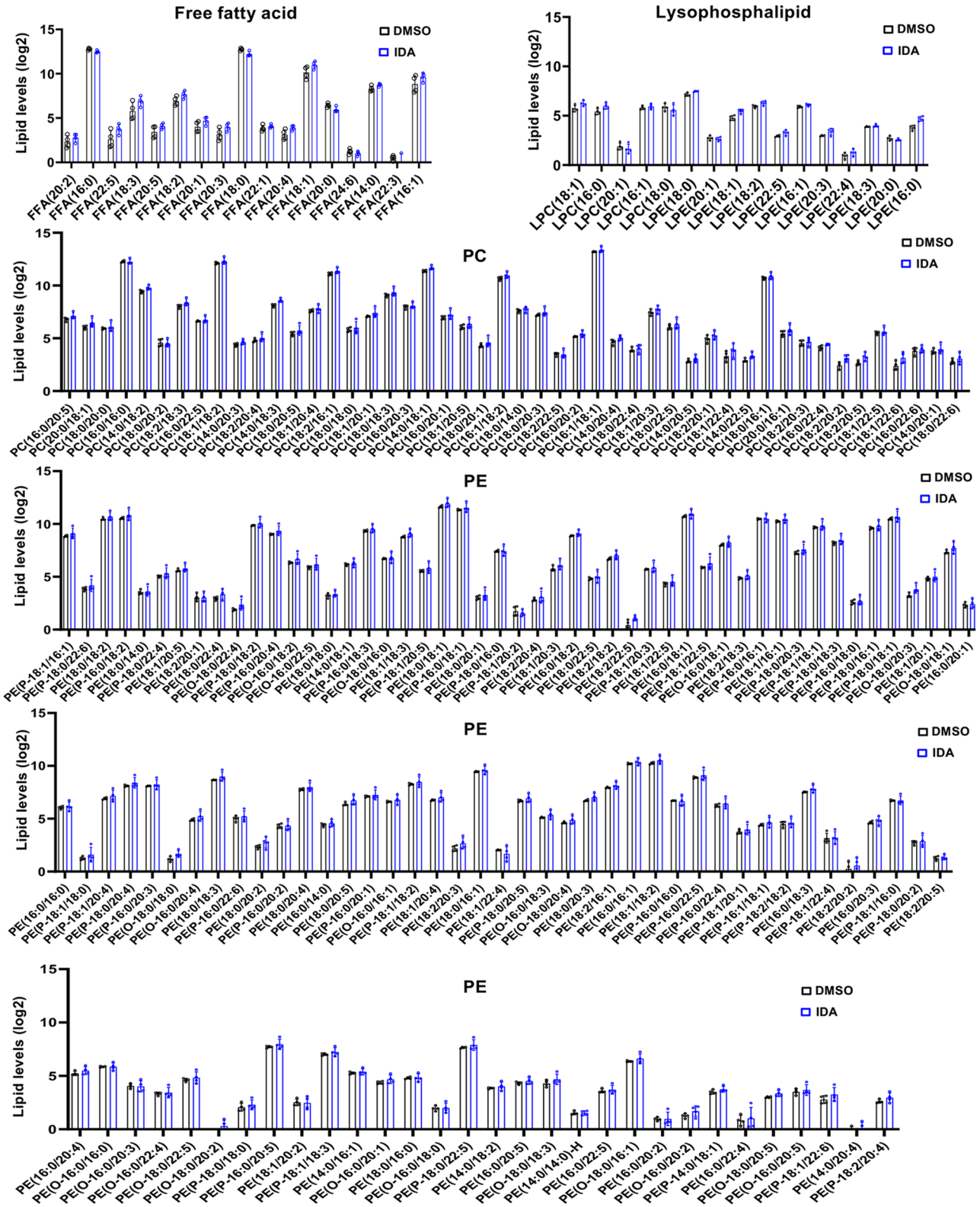

Extended Data Fig. 6 | Supplementation with IDA does not alter the phospholipid composition. Lipidomic profile (free fatty acids, lysophosphalipid, phosphatidylethanolamine (PE), phosphatidylcholine (PC), including plasmenyl (O) and plasmanyl (P) lipids) in HT29 cells supplemented with IDA (50 μM). Data and error bars are mean ± s.d., n = 4 independent repeats. All P values were calculated using two-tailed unpaired Student's t-test.

https://doi.org/10.1038/s41556-023-01314-6

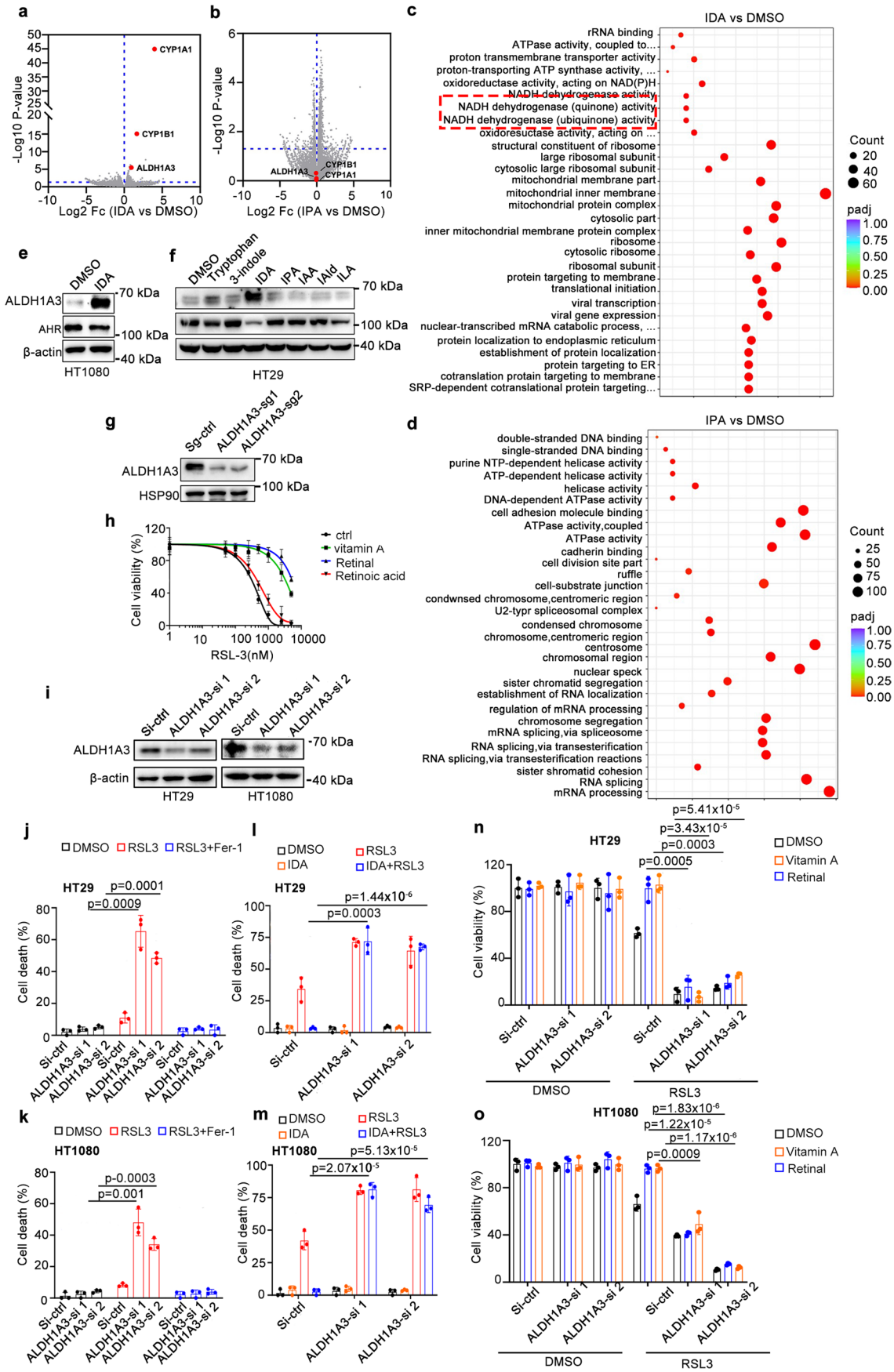

Extended Data Fig. 7 | See next page for caption.

https://doi.org/10.1038/s41556-023-01314-6

Extended Data Fig. 7 | ALDH1A3 is a transcriptional target of AHR and IDA mediated- ferroptosis inhibition is dependent of ALDH1A3. (a, b) Volcano plots of RNA-SEQ data in HT29 cells supplemented with IDA (50 μM) (a) and IPA (50 μM) (b). (c, d) Go enrichment of IDA (50 μM) (c) treated- and IPA (50 μM) (d) treated-HT29 cells, highlighting that the pathway of NADH dehydrogenase (quinone/ubiquinone) activity is specifically enriched in IDA-treated cells. (e) Western blotting showing levels of ALDH1A3 in HT1080 upon IDA (50 μM) treatment. (f) Western blot analysis of ALDH1A3 expression in HT29 cells upon supplementation of tryptophan metabolites. Tryptophan (50 μM), IDA (50 μM), IPA (50 μM), 3-indole (50 μM), Indole-3-acetic acid (IAA, 50 μM), indole-3-aldehyde (IAld, 50 μM) and Indole-3-lactic acid (ILA, 50 μM). (g) Western blot analysis of HT29 cells expressing sg-ctrl or sg-ALDH1A3. (h) Cell viability in HT29 cells treated with RSL3, vitamin A (10 μM), retinal (10 μM) or retinoic acid (10 μM) for 24 h. (i) Western blot analysis of HT29 and HT1080 cells transfected with ALDH1A3 siRNA. (j, k) Cell death of HT29 (j) and HT1080 cells (k) expressing si-ctrl or si-ALDH1A3 treated with RSL3 and Fer-1 (1 μM) for 8 h. (l, m) Cell death of HT29 (l) and HT1080 cells (m) expressing si-ctrl or si-ALDH1A3 treated with RSL3 and IDA (50 μM) for 8 h. (n, o) Cell viability in HT29 (n) and HT1080 cells (o) expressing si-ctrl or si-ALDH1A3 treated with RSL3, vitamin A (10 μM) or retinal (10 μM) for 24 h. The Western blot experiments were repeated three times independently with similar results in e-g and i. Data and error bars are mean ± s.d., n = 3 biological independent experiments in a, b, h and j-o. All P values were calculated using two-tailed unpaired Student's t-test.

https://doi.org/10.1038/s41556-023-01314-6

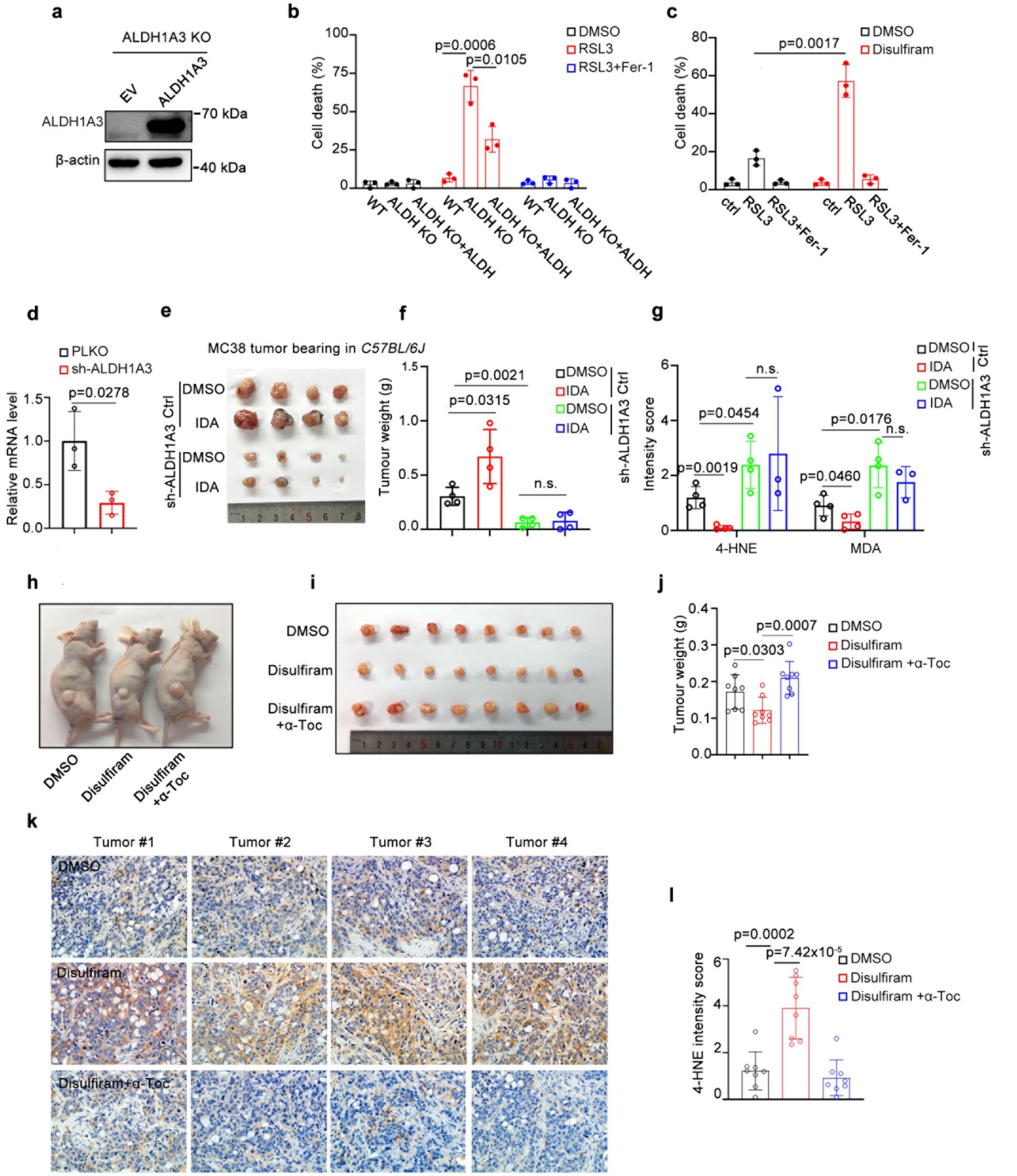

Extended Data Fig. 8 | See next page for caption.

https://doi.org/10.1038/s41556-023-01314-6

Extended Data Fig. 8 | ALDH1A3 promotes tumour growth *in vivo* by ferroptosis inhibition. (a) Western blot analysis of ALDH1A3 expression in HT29 ALDH1A3 KO cells with ectopic expression of ALDH1A3. (b) Cell death of HT29 ALDH1A3 KO cells with ectopic expression of ALDH1A3 treated with RSL3 (5 μM) and IDA (50 μM) for 8 h. (c) Cell death of HT29 cell upon disulfiram (10 μM), RSL3 (5 μM) and Fer-1 (1 μM) for 8 h. (d) Detection of the expression of ALDH1A3 in MC38 cells transfected with shRNA for ALDH1A3. (e) Representative images of *C57BL/6 J* mice bearing tumours of MC38 cells transfected with indicated shRNA. n = 4 independent tumours. (f) Tumour weight of MC38 sh-ctrl or ALDH1A3-shRNA cells upon IDA treatment (50 mg/kg). n = 4 independent tumours. (g) Immunohistochemistry scoring of 4-HNE and MDA in the tumour samples from (f). Scale bars, 50 μm. n = 4 independent tumours except for n = 3 in the group of ALDH1A3-shRNA cells treated with IDA. (h) Representative images of xenograft tumours of HT29 cells treated with disulfiram (50 mg/kg) and α-Toc (10 mg/kg). (i, j) xenograft tumours (i) of HT29 cells treated with disulfiram (50 mg/kg) and α-Toc (10 mg/kg). Tumour weights were scored (j). n = 8 independent tumours. (k, l) Immunohistochemistry staining of 4-HNE (k) in the tumour samples from (i). Scale bars, 50 μm. (l) 4-HNE intensity was scored. n = 8 independent tumours. The Western blot experiments were repeated three times independently with similar results in a. Data and error bars are mean ± s.d., n = 3 biological independent experiments in b-d. All P values were calculated using two-tailed unpaired Student's t-test.

https://doi.org/10.1038/s41556-023-01314-6

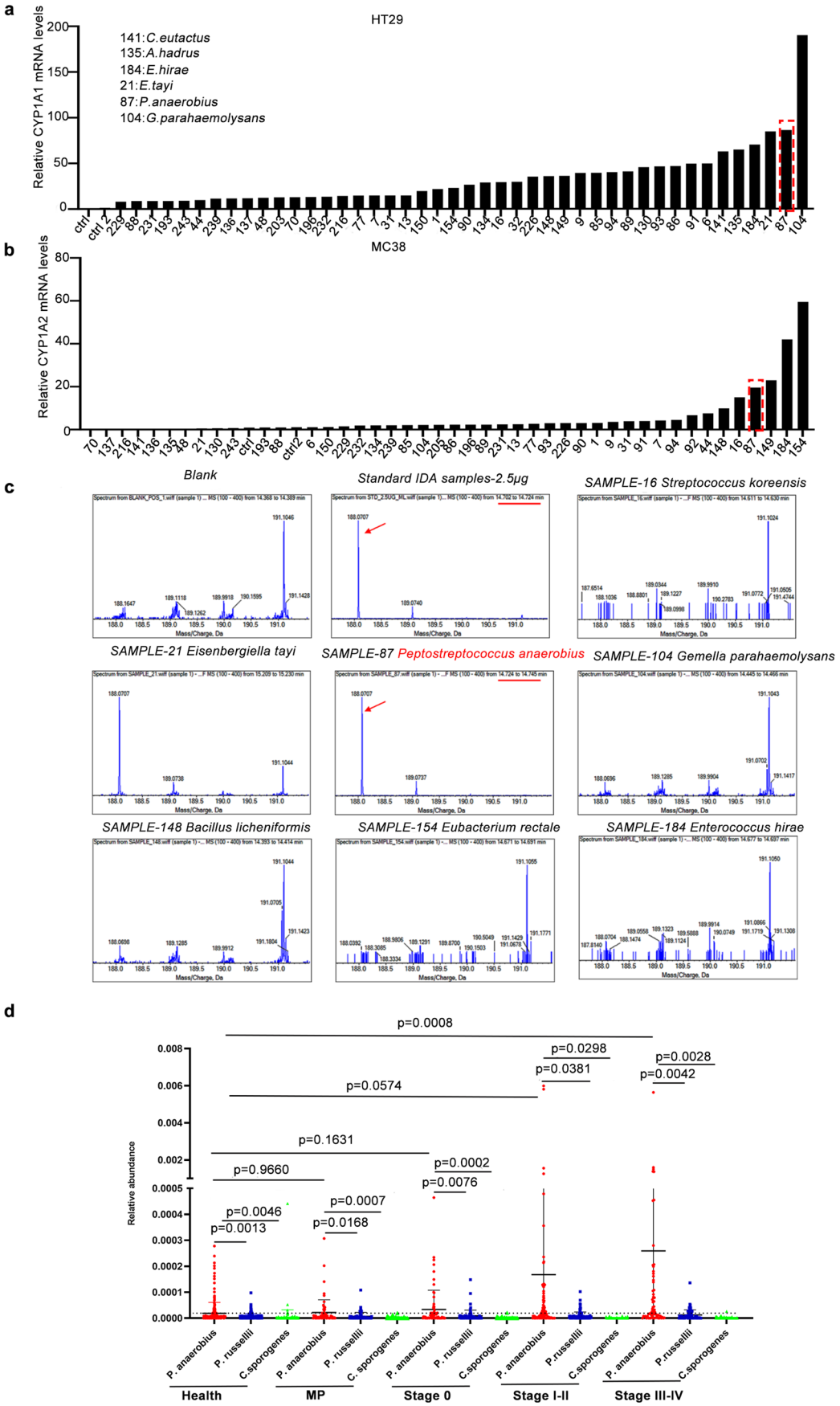

Extended Data Fig. 9 | See next page for caption.

https://doi.org/10.1038/s41556-023-01314-6

Extended Data Fig. 9 | *P.anaerobius* is the major contributor of IDA biosynthesis. (a, b) The change of mRNA levels of CYP1A1 and CYP1A2 in HT29 (a) and MC38 cells (b) upon treatment with the supernatants derived from the indicated strains. Sample 87 indicates *P.anaerobius*. (c) Strains that significantly upregulated cyp1a1 and cyp1a2 were subjected to detect IDA concentration by LC-MS. Sample 87 indicates *P.anaerobius*. (d) The relative abundance of *P.anaerobius, P.russellii* and *C. sporogenes* in CRC patients in different histological groups. Health: n = 111, MP: n = 67, Stage 0: n = 73, Stage I-II: n = 111 and Stage III-IV: n = 74.

https://doi.org/10.1038/s41556-023-01314-6

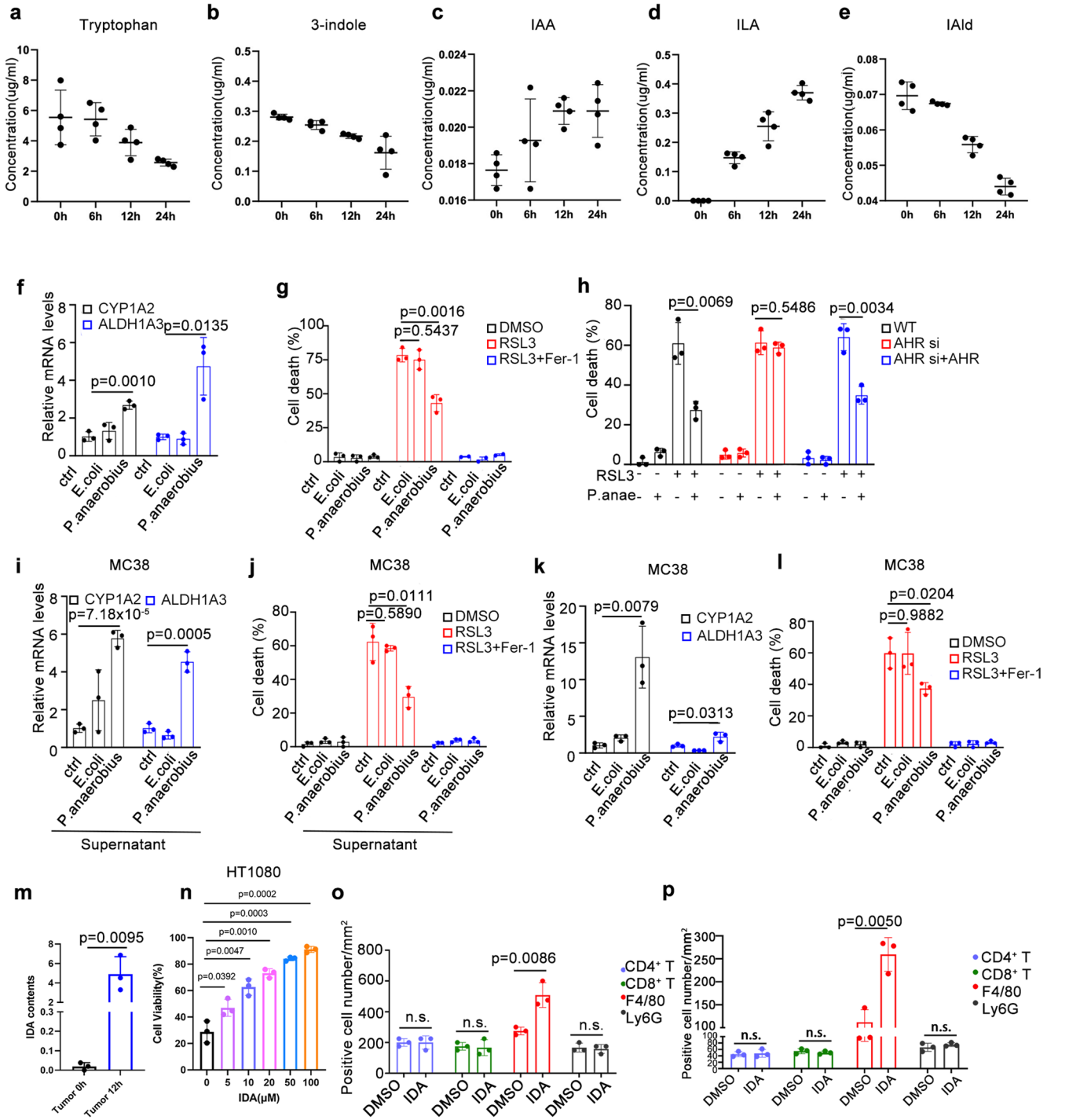

Extended Data Fig. 10 | *P. anaerobius* accelerates colorectal tumorigenesis via generation of IDA. (a-e) LC-MS analysis of the contents of tryptophan(a), 3-indole(b), IAA(c), ILA(d) and IAld (e) contents derived from *P. anaerobius* supernatant with indicated times. n = 4 biological independent experiments. (f) Relative mRNA levels of CYP1A1 and ALDH1A3 in HT29 cells upon co-culture with *E.coli* or *P. anaerobius*. (g) Cell death of HT29 cells treated with RSL3 (5 μM) for 8 h following co-culture with *E.coli* or *P. anaerobius*. (h) Cell death of MC38 cells transfected with AHR siRNA upon ectopic expression of AHR treated with RSL3 (5 μM) for 8 h following co-culture with *P. anaerobius*. (i) Relative mRNA levels of CYP1A2 and ALDH1A3 in MC38 cells supplemented with supernatant from *E.coli* or *P. anaerobius*. (j) Cell death of MC38 cells treated with RSL3 (5 μM) for 8 h following supplementation with supernatant from *E.coli* or *P. anaerobius*. (k) Relative mRNA levels of CYP1A2 and ALDH1A3 in MC38 cells upon co-culture with *E.coli* or *P. anaerobius*. (l) Cell death of MC38 cells treated with RSL3 (5 μM) for 8 h following co-culture with *E.coli* or *P. anaerobius*. (m) MC38 cells-tumour bearing in *C57BL/6 J* mice was established and collected tumor samples 12 h after *P.anaerobius* intratumoral injection, followed by detecting the content of IDA in the tumor samples by LC-MS. n = 3 independent mice. (n) Cell viability of HT1080 upon RSL3 and IDA treatment. (o) Immunofluorescence staining of $CD4^+$T, $CD8^+$ T, macrophage (F4/80) and neutrophils (Ly6G) cells of intestinal orthotopic tumorigenesis upon IDA (i.p 50 mg/kg) treatment in AOM/DSS model of Colitis-associated cancer and positve cells was calculated. n = 3 independent mice. (p) Immunofluorescence staining of $CD4^+$ T, $CD8^+$ T, macrophage (F4/80) and neutrophils (Ly6G) cells in the subcutaneous tumour samples with IDA treatment (i.p,50 mg/kg) in *C57BL/6 J* mice and positve cells was calculated. n = 3 independent mice. Data and error bars are mean ± s.d., n = 3 biological independent experiments in f-l and n. All P values were calculated using two-tailed unpaired Student's t-test.

nature portfolio

Corresponding author(s): Bo Chu

Last updated by author(s): Oct 31, 2023

Reporting Summary

Nature Portfolio wishes to improve the reproducibility of the work that we publish. This form provides structure for consistency and transparency in reporting. For further information on Nature Portfolio policies, see our Editorial Policies and the Editorial Policy Checklist.

Statistics

For all statistical analyses, confirm that the following items are present in the figure legend, table legend, main text, or Methods section.

n/a	Confirmed
☐	☒ The exact sample size (*n*) for each experimental group/condition, given as a discrete number and unit of measurement
☐	☒ A statement on whether measurements were taken from distinct samples or whether the same sample was measured repeatedly
☐	☒ The statistical test(s) used AND whether they are one- or two-sided *Only common tests should be described solely by name; describe more complex techniques in the Methods section.*
☒	☐ A description of all covariates tested
☒	☐ A description of any assumptions or corrections, such as tests of normality and adjustment for multiple comparisons
☐	☒ A full description of the statistical parameters including central tendency (e.g. means) or other basic estimates (e.g. regression coefficient) AND variation (e.g. standard deviation) or associated estimates of uncertainty (e.g. confidence intervals)
☐	☒ For null hypothesis testing, the test statistic (e.g. *F*, *t*, *r*) with confidence intervals, effect sizes, degrees of freedom and *P* value noted *Give P values as exact values whenever suitable.*
☒	☐ For Bayesian analysis, information on the choice of priors and Markov chain Monte Carlo settings
☒	☐ For hierarchical and complex designs, identification of the appropriate level for tests and full reporting of outcomes
☐	☒ Estimates of effect sizes (e.g. Cohen's *d*, Pearson's *r*), indicating how they were calculated

Our web collection on statistics for biologists contains articles on many of the points above.

Software and code

Policy information about availability of computer code

Data collection

Becton Dickinson FACS Calibur machine was used to collect flow cytometry data.
Mithras LB940 microplate reader (Berthold Technologies) was used to evaluate compouds resistance to oxidation.
The UHPLC-MS/MS platform consisting of an EXIONLC System (Sciex), equipped with a ZORBAX Eclipse Plus C18 Rapid Resolution HD 2.1× 50 mm 1.8-Micron was used to collect CoQ and CoQH2 data.
Sytox Green positive cells were calculated by an inverted fluorescence microscope (Olympus).
Immunohistochemical sections were photographed by upright microscope (Olympus).
Human colon cancer cell organoids were captured by an inverted fluorescence microscope (Nikon).
QPCR was performed on CFX-Connect machine (BIO-RAD).
Accurate mass LC/MS was performed on an AB TripleTOF operating in IDA mode as previously described (Marta Wlodarska et al., 2017).
A SCIEX ExionLC series UHPLC System was used to detect the abundance of phospholipids.

Data analysis	GraphPad 8 were used for bar graphs output and statistical analysis. FlowJo_V10 was used for flow cytometry data analysis. DADA2-package integrated in QIIME2 (Quantitative Insights Into Microbial Ecology2) was used to analyze 16S rRNA gene sequencing of fecal microbiota. IDA content was analyzed using PeakView 1.2 software. Image pro-plus and Image J software were used to perform the quantitative analysis of pictures. Organiods were visualized by NIS Elements Viewer software 5.21. The software and algorithms for data analysis used in this study are all well-established from previous work. All software and custom arguments are included in Methods section. There is no unreported algorithm used in this manuscript.

For manuscripts utilizing custom algorithms or software that are central to the research but not yet described in published literature, software must be made available to editors and reviewers. We strongly encourage code deposition in a community repository (e.g. GitHub). See the Nature Portfolio guidelines for submitting code & software for further information.

Data

Policy information about availability of data

All manuscripts must include a data availability statement. This statement should provide the following information, where applicable:

- Accession codes, unique identifiers, or web links for publicly available datasets
- A description of any restrictions on data availability
- For clinical datasets or third party data, please ensure that the statement adheres to our policy

The survival curve data of AHR gene expression data in human cancer tissues were derived from TCGA database and in human cancer cell lines from CCLE (https://portals.broadinstitute.org/ccle/). The correlation of AHR and ALDH1A3 in human cancer tissues were derived from GEPIA (http://gepia2.cancer-pku.cn/). The expression of AHR and ALDH1A3 were derived from Oncomine (https://www.oncomine.org/). CHIP-SEQ data of AHR is available from the database (http://chip-atlas.org/). RNA-SEQ data are provided as supplementary tables. Source data are provided with this paper.

Human research participants

Policy information about studies involving human research participants and Sex and Gender in Research.

Reporting on sex and gender	The fecal samples for P. anaerobius enrichments and IDA contents were collected from 35-75 years-old male and female CRC patients derived from the First Affiliated Hospital of USTC and corresponding age and sex healthy controls selected from the Physical Examination Center of the First Affiliated Hospital of USTC. The study was approved by the Ethics Committee of USTC. The number of participants in these experiments is detailed described in the corresponding figure legends.
Population characteristics	35-75 years-old CRC patients derived from the First Affiliated Hospital of USTC and corresponding age healthy controls.
Recruitment	Patients were recruited when for the first time diagnosed CRC without any treatment.
Ethics oversight	The study was approved by the Ethics Committee of USTC.

Note that full information on the approval of the study protocol must also be provided in the manuscript.

Field-specific reporting

Please select the one below that is the best fit for your research. If you are not sure, read the appropriate sections before making your selection.

☒ Life sciences ☐ Behavioural & social sciences ☐ Ecological, evolutionary & environmental sciences

For a reference copy of the document with all sections, see nature.com/documents/nr-reporting-summary-flat.pdf

Life sciences study design

All studies must disclose on these points even when the disclosure is negative.

Sample size	Sample size, number of replicates, error bars and statistical test were chosen based experiments and stated in each figure legends. All the experiments including technical replicates were repeated at least three independent times. No statistical methods were used to pre-determine sample sizes.
Data exclusions	No data were excluded from the analyses, and biological samples were excluded from the study only if sample preparation or data acquisition failed.
Replication	All experiments were repeated at least three independent times for quantitative analysis. Details are provided in each figure legend.
Randomization	For both in vitro and in vivo experiments, samples/ animals were assigned to experimental groups using simple randomization.

Blinding	The investigators were not blinded to allocation during experiments and outcome assessment since blinding is not relevant to this study. Interpretation of the results was based solely on objective measures and did not rely on subjective evalution by the authors.

Reporting for specific materials, systems and methods

We require information from authors about some types of materials, experimental systems and methods used in many studies. Here, indicate whether each material, system or method listed is relevant to your study. If you are not sure if a list item applies to your research, read the appropriate section before selecting a response.

Materials & experimental systems

n/a	Involved in the study
☐	☒ Antibodies
☐	☒ Eukaryotic cell lines
☒	☐ Palaeontology and archaeology
☐	☒ Animals and other organisms
☒	☐ Clinical data
☒	☐ Dual use research of concern

Methods

n/a	Involved in the study
☒	☐ ChIP-seq
☐	☒ Flow cytometry
☒	☐ MRI-based neuroimaging

Antibodies

Antibodies used

AHR (1:1000; 83200; Cell Signaling Technology),
ALDH1A3 (1:1000, 25167-1-AP, Proteintech),
NRF2 (1:1000; 16936-1-AP; Proteintech),
GPX4(1:1000; ab125066; Abcam),
xCT/SLC7A11 (1:1000; 12691; Cell Signaling Technology),
Flag-M2 (1:1000; F1804; Sigma-Aldrich),
Myc-Tag(1:1000, 2276S; Cell Signaling Technology),
NQO1 (1:1000; 11451-1-AP; Proteintech),
DHODH(1:1000; 14877-1-AP; Proteintech),
GCH1(1:1000; 28501-1-AP; Proteintech),
FSP(1:1000; 20886-1-AP; Proteintech),
GAPDH (1:2000; sc-47724; Santa Cruz Biotechnology),
β-actin(1:3000; 66009-1-AP; Proteintech),
HSP90(1:3000, TA-12, ZSGB-BIO),
Tubulin(1:3000, TA347064, ZSGB-BIO) ,
4-HNE (1:200, ab46545, Abcam),
MDA (1:200, JAI-MMD-030N, Adipogen),
8-OHDG(1:200, ab48508, Abcam)
peroxidase-conjugated goat anti-rabbit or mouse IgG(H+L) secondary antibody(1:5000, 111-035-003 and115-035-003, Jackson ImmunoResearch Laboratories)

Validation

All antibodies used in our study have been validated and detailed information could be obtained the website from manufactures as listed below. Information about usage, validation and citation are available from the product page.
AHR: https://www.cellsignal.cn/products/83200.
ALDH1A3: https://www.ptgcn.com/products/ALDH1A3-Antibody-25167-1-AP.htm
NRF2:https://www.ptgcn.com/products/NFE2L2,NRF2-Antibody-16396-1-AP.htm
GPX4: https://www.abcam.cn/ ab125066.html
xCT/SLC7A11: https://www.cellsignal.cn/products/12691.
Flag-M2: https://www.sigmaaldrich.cn/CN/zh/product/sigma/f1804
Myc: https://www.cellsignal.cn/products/2276
NQO1: https://www.ptgcn.com/products/NQO1-Antibody-11451-1-AP.htm
FSP1: https://www.ptgcn.com/products/AIFM2-Antibody-20886-1-AP.htm
DHODH: https://www.ptgcn.com/products/DHODH-Antibody-14877-1-AP.htm
GCH1: https://www.ptgcn.com/products/GCH1-Antibody-28501-1-AP.htm
GAPDH: https://www.scbt.com/zh/p/gapdh-antibody-0411
β-actin: https://www.ptgcn.com/products/Pan-Actin-Antibody-66009-1-Ig.htm
HSP90: http://www.zsbio.com/product/TA-12
Tubulin: http://www.zsbio.com/product/TA347064
4-HNE: https://www.abcam.com/products/primary-antibodies/4-hydroxynonenal-antibody-ab46545.html
MDA: https://us.vwr.com/store/product/21875343/anti-mda-monoclonal-antibody-clone-1f83
8-OHDG: https://www.abcam.com/products/primary-antibodies/8-hydroxy-2-deoxyguanosine-antibody-n451-ab48508.html
peroxidase-conjugated goat anti-rabbit secondary antibody: https://www.jacksonimmuno.com/catalog/products/111-035-003
peroxidase-conjugated goat anti-mouse secondary antibody: https://www.jacksonimmuno.com/catalog/products/115-035-003

Eukaryotic cell lines

Policy information about cell lines and Sex and Gender in Research

Cell line source(s)	HT29, MC38, HEK293T, HT1080 and 786-O cancer cell lines were acquired from the Cell Banks of Type Culture Collection of Chinese Academy of Sciences (Shanghai, China) and have been proved to be negative for mycoplasma contamination. No cell lines used in this work were listed in the ICLAC database
Authentication	Cell line were not authenticated.
Mycoplasma contamination	All cell lines tested negative for mycoplasma contamination.
Commonly misidentified lines (See ICLAC register)	No ICLAC cell line was used in this study.

Animals and other research organisms

Policy information about studies involving animals; ARRIVE guidelines recommended for reporting animal research, and Sex and Gender in Research

Laboratory animals	The nude and C57BL/6J male mice at 6-8 week old were purchased from Charles River Laboratories. Male C57BL/6J ApcMin/+ mice (8 weeks old) was purchased from Gempharmatech company (Jiangsu, China). 12-wk-old male Germ Free C57BL/6J mice were purchased from Cyagen Biosciences (Suzhou, China).
Wild animals	No wild animals involved in this study.
Reporting on sex	Male mice were used in this study
Field-collected samples	No field collected samples were used in the study.
Ethics oversight	All the xenograft model experiments were performed in accordance with a protocol approved by the Policy on the Ethical Use and Care of Animals (School of Basic Medical Sciences, Cheeloo College of Medicine, Shandong University) and (school of Basic Medical Sciences, Division of Life Sciences and Medicine, University of Science and Technology of China) .

Note that full information on the approval of the study protocol must also be provided in the manuscript.

Flow Cytometry

Plots

Confirm that:

☒ The axis labels state the marker and fluorochrome used (e.g. CD4-FITC).

☒ The axis scales are clearly visible. Include numbers along axes only for bottom left plot of group (a 'group' is an analysis of identical markers).

☒ All plots are contour plots with outliers or pseudocolor plots.

☒ A numerical value for number of cells or percentage (with statistics) is provided.

Methodology

Sample preparation	Cells cultured in 24-well plate were harvested and washed with PBS, then resuspended with PBS containing 5 μM C-11 BODIPY 581/591 dye (D3861, Thermo Fisher Scientific) and incubated in the tissue culture incubator for 30 min. Cells were then washed twice with PBS followed by resuspending in 200 μl PBS for flow cytometry analysis.
Instrument	ROS levels were analyzed using a Becton Dickinson FACS Calibur machine through the FL1 channel.
Software	The data were analyzed using FlowJo V10 software.
Cell population abundance	at least 5,000 cells were analyzed in each sample.
Gating strategy	Drawing gate (FSC-area Vs SSC-Area) was used to collect initial cells population, then removing the adherent cells and only single cell was used for analysis.

☒ Tick this box to confirm that a figure exemplifying the gating strategy is provided in the Supplementary Information.